# On the Estimation of Physical Roughness of Sea Ice in the Canadian Arctic Archipelago using Synthetic Aperture Radar

by

Silvie Cafarella
B.Sc., University of Victoria, 2016

A Thesis Submitted in Partial Fulfillment
of the Requirements for the Degree of

MASTER OF SCIENCE

in the Department of Geography

**Supervisory Committee**

# On the Estimation of Physical Roughness of Sea Ice in the Canadian Arctic Archipelago using Remote Sensing

by

Silvie Cafarella
B.Sc., University of Victoria, 2016

**Supervisory Committee**

Dr. Randy Scharien, (Department of Geography)
**Supervisor**

Dr. David Atkinson, (Department of Geography)
**Departmental Member**

# Abstract

Sea ice surface roughness is a geophysical property which can be defined and quantified on a variety scales, and consequently affects processes across various scales. The sea ice surface roughness influences various mass, gas, and energy fluxes across the ocean-sea ice-atmosphere interface. Utilizing synthetic aperture radar (SAR) data to understand and map sea ice roughness is an active area of research. This thesis provides new techniques for the estimation of sea ice surface roughness in the Canadian Arctic Archipelago using synthetic aperture radar (SAR). Estimating and isolating sea ice surface properties from SAR imagery is complicated as there are a number of sea ice and sensor properties that influence the backscattered energy. There is increased difficulty in the melting season due to the presence of melt ponds on the surface, which can often inhibit interactions from the sensor to the sea ice surface as shorter microwaves cannot penetrate through the melt water. An object-based image analysis is here used to quantitatively link the winter first-year sea ice surface roughness to C-band RADARSAT-2 and L-band ALOS-2 PALSAR-2 SAR backscatter measured at two periods: winter (pre-melt) and advanced melt. Since the sea ice in our study area, the Canadian Arctic Archipelago, is landfast, the same ice can be imaged using SAR after the surface roughness measurements are established. Strong correlations between winter measured surface roughness, and C- and L-band SAR backscatter acquired during both the winter and advanced melt periods are observed. Results for winter indicate: (1) C-band HH-polarization backscatter is correlated with roughness ($r=0.86$) at a shallow incidence angle; and (2) L-band HH- and VV-polarization backscatter is correlated with roughness ($r=0.82$) at a moderate incidence angle. Results for advanced melt indicate: (1) C-band HV/HH polarization ratio is correlated with roughness ($r=-0.83$) at shallow incidence angle; (2) C-band HH-polarization backscatter is correlated with roughness ($r=0.84$) at shallow incidence angle for deformed first-year ice only; and (3) L-band HH-polarization backscatter is correlated with roughness ($r=0.79$) at moderate incidence angle. Retrieval models for surface roughness are developed and applied to the imagery to demonstrate the utility of SAR for mapping roughness, also as a proxy for deformation state, with a best case RMSE of 5 mm in the winter, and 8 mm during the advanced melt.

# Table of Contents

# List of Tables

# List of Figures

# Acknowledgments

I would like to gratefully acknowledge the logistical and financial support from my supervisor, Dr. Randy Scharien. I would also like to thank Dr. David Atkinson for his academic support and encouragement as a member of my Master thesis committee. I would also like to thank Dr. Edwin Nissen for fulfilling the role of external examiner for my Master oral examination. I am thankful to John Fowler, Dr. Dennis Jelinski, and Dr. Johannes Feddema of the Department of Geography for providing support at the department level. I am thankful to the administrative staff of the Geography Department and Faculty of Graduate Studies for logistics.

I am thankful to Dr. Christian Haas, Dr. Torsten Geldsetzer, and Dr. Stephen Howell for their valuable assistance with the manuscript in Chapter 3. I would also like to thank Christian Haas and Stephen Howell for providing data used in Chapter 3. I am thankful to C-CORE for hosting me and providing me insight on earth observations techniques used in the Arctic environment. Discussions on radar remote sensing with the C-CORE remote sensing and GIS analysts were very valuable. Discussions on laser scanning data with Alec Casey were also very useful. I would like to personally thank Terri Evans and Jessica Fitterer for their technical expertise and support. Lastly, I am grateful for all members of the ICE lab with their constant support and advice, including Sasha Nasonova, Becky Segal, Aikaterini Tavri, Parnian Rezania, and Vishnu Nandan.

# Chapter 1 : Introduction

## 1.1. Rationale and Context

Sea ice exists as a thin layer of the cryosphere which interacts continuously with the underlying oceans and overlaying atmosphere. Sea ice shelters the ocean from atmospheric forcing by damping heat, mass, and momentum fluxes (Thomas 2017; NSIDC 2019). The ocean currents and atmospheric winds drive the sea ice cover to drift freely, as well as converge with and diverge from adjacent ice floes. Each component in the sea ice-ocean-atmosphere system is inherently linked and highly sensitive to changes from internal and external forcings (i.e. radiative forcing).

In recent decades, there was been a drastic decrease in extent and thickness of the Arctic sea ice cover (Kwok and Rothrock 2009; Comiso 2011; Maslanik *et al.* 2011; Stroeve *et al.* 2012; Stroeve *et al.* 2014; Landy *et al.* 2015; Comiso2017). The apparent decrease suggests that the Arctic sea ice cover, once predominantly old, thick perennial sea ice, is transitioning to a thinner cover of seasonal ice. As the extent, age, and thickness of the sea ice cover continues to change, the resulting sea ice topography will change. Consequently, the sea ice topography reflects the history of thermodynamic and dynamic processes acting upon the sea ice cover. To understand changes occurring in the sea ice topography, and its effects on other processes at the surface, it is necessary to describe the nature of the surface and define its properties of topographic relief. The sea ice topography can be characterized by measurements of surface roughness.

Sea ice surface roughness is the result of surface-atmosphere interactions, ice motion, and ice surface melt. Roughness provoked by ice motion is dependent on wind

speed and direction, ocean currents and coastline interactions (Thomas 2017; Rothrock and Thornlike 2018). These thermodynamic and dynamic processes occur across multiple scales; therefore, surface roughness is a highly-scale dependent variable, ranging from centimeter-scale surface features and meter-scale ice floes to kilometre-scale regions. The various scales of sea ice surface roughness become increasingly important and influential when deriving surface roughness parameters from *in situ* and remotely sensed data. Due to the remote and harsh nature of the Arctic environment, remote sensing techniques have been a valuable tool for monitoring the state of the sea ice cover over space and time. However, sea ice surface roughness is a challenging parameter to define, let alone retrieve. Surface topography measurements from satellite remote sensors have been too coarse to characterize spatial or temporal changes in the sea ice surface. Low elevation airborne sensors (i.e. LiDAR) can provide fine scale measurements over sea ice, but the overall spatial and temporal coverage is sparse. In recent decades, satellite remote sensors are being launched with finer spatial and temporal resolutions.

This research establishes quantitative links between the physical surface roughness of sea ice and Synthetic Aperture Radar (SAR) backscatter in both winter and summer months representing winter (pre-melt) and advanced melt conditions, respectively. A quantitative link would enable regional measurements of surface roughness from satellite imagery. Surface roughness estimates of sea ice are crucial in understanding the parameters of an electromagnetic surface, identifying ice types, surface temperatures, surface drag coefficients, and identification of navigational hazards. This research will contribute to the development of improved monitoring techniques for the rapidly changing Arctic sea ice cover.

## 1.2. Objectives

The overarching goal of this thesis is to develop SAR satellite-based techniques to quantitatively map the physical sea ice surface roughness across the physically relevant scales (cm to m), with the potential to implement the technique over larger areas. To develop SAR satellite-based retrievals models, it is essential to explore and establish the extent to which the level of deformation, expressed as a surface roughness measurement, influences the radar backscatter with different combinations of radar system parameters (i.e. frequency, incidence angle, polarization). The research will also address how seasonal differences in surface cover influence the link between surface roughness and detected backscatter. Surface roughness is not the sole target parameter influencing the backscatter microwave radiation. The detected backscatter is affected by both the geophysical structure and environmental, thermo-physical state of the snow and sea ice. The surface cover of sea ice undergoes a drastic change when air temperatures warm and the ice and snow begin to thaw. Relationships between the dry surface cover and backscatter in the winter months do not entirely persist in the advanced melt period, in particular when surface melt ponds are present. However, it is of considerable interest, in the context of understanding what sea ice geophysical information can be retrieved during advanced melting conditions, to explore the relationships between winter-derived surface roughness, and advanced melt period measured backscatter. Additionally, the backscatter detected from a ponded area will differ significantly at each frequency due to varying penetration capabilities. This thesis will address the following questions:

1. How does the physical surface roughness of sea ice influence SAR backscatter in the winter months?

2. To what extent is it possible to quantitatively link the physical surface roughness to radar backscatter? Is it possible to accurately design an inverse retrieval model of surface roughness measurements from SAR backscatter?

3. How does the relationship between surface roughness and SAR backscatter change during the advanced melt period? Is it possible to link surface roughness measurements and SAR backscatter during advanced melt?

## 1.3. Thesis Structure

This thesis contains four chapters. Chapter-1 provides a rationale and broad review of this research and its scientific significance. Chapter-2 introduces the reader to a comprehensive background and literature review, which explores the physical processes that create the surface roughness of sea ice, how the surface roughness influences the ocean-ice-atmosphere dynamics, and how remote sensing instruments can be used to define the surface roughness of sea ice. Chapter-3 is a research paper designed to address the thesis objectives; therefore it contains details on the study area, data, analytical approach, and results. This chapter includes content also used to publish a paper in the Canadian Journal of Remote Sensing. The contributions from authors are in the Appendix. Chapter 4 summarizes the thesis and its findings and makes recommendations for future research.

# Chapter 2 : Background and Literature Review

## 2.1. Sea Ice Roughness

Based on the World Meterological Organization (WMO) definitions, sea ice topography is described at three spatial scales, micro-, meso-, and macro-scale. Micro-scale topography (<0.1m) is defined as the millimeter and centimeter scale variations in vertical relief, including bare ice, snow grains, frost flowers, and small snow drift features (Paterson *et al.,* 1991; NSIDC, 2017; Manninen, 1997). Meso-scale topography (0.1-100m) describes larger fluctuations in the sea ice topography, including larger snow drift features, melt ponds, and deformed ice features, such as pressure ridges and hummocks. Meso-scale roughness undulations and features influence the atmospheric drag coefficient and drive differential rates of sea ice melt between locations and years. Lastly, macro-scale topography (>100m) characterizes sea ice floes and floe distribution. Macro-scale surface roughness can be used to predict the pattern and distribution of melt ponds across the Arctic basin. Surface roughness, the variation in topography, is a geophysical property which can be defined and quantified on a variety scales, and consequently affects processes across various scales. In terms of Arctic sea ice research, the definition of sea ice surface roughness has shifted to reflect how instruments are manipulated to define or describe the sea ice topography.

Sea ice surface roughness plays a key role in the evolution of the ice cover, most notably, the summer melt pond fraction, which quantifies the spatial coverage of melt water on the ice surface (Eicken *et al.* 2004; Perovich and Polashenski 2012). During the melt season, the surface becomes heterogeneous with the melting of snow and formation

of melt ponds. The depth and geometry of these melt ponds are determined by the local sea ice surface topography, which is often governed by the ice type. The most common distinction of ice types is whether the ice formed in the current year (i.e. first-year ice) or has survived at least one melting season (i.e. multiyear ice). These ice types can be further characterized based on their thickness and level of deformation. Level first-year (LFYI) promotes shallow, spatially extensive ponding, whereas, rougher, deformed first-year (DFYI) and multiyear ice (MYI) promote deeper, but less spatially extensive depressions for melt water (Morassutti and Ledrew 1996; Fetterer and Untersteiner 1998). Furthermore, sea ice topography modulates the turbulent fluxes of momentum (drag coefficients) over (i.e. air-ice), as well as under the ice surface (i.e. water-ice) (Steiner *et al.* 1999; Petty *et al.* 2017). These fluxes can be related to the topography through the concept of the aerodynamic roughness length, which is defined by the height above a surface at which the wind speed theoretically becomes zero. A rougher surface should produce larger turbulent eddies, therefore it is assumed that the surface stress increases with increasing surface roughness (Arya 1973; Arya 1975; Petty *et al.* 2017). The total atmospheric drag coefficients are divided into contributions from frictional skin drag due to micro-scale roughness and form drag acting on discrete surface obstacles (i.e. pressure ridges and melt ponds) (Arya 1973; Arya 1975; Petty *et al* 2017). Moreover, sea ice roughness is also expected to be closely related to the ice thickness because of isostasy, which theorizes that the elevation of the ice is a function of its thickness and density (Peterson *et al.,* 2008). These relationships and processes will be discussed in in further detail after an overview of the thermodynamic and dynamic processes that create roughness in the Canadian Arctic Archipelago.

## 2.2. Physical Processes Creating Roughness

### 2.2.1. Thermodynamic Processes

Sea ice growth season begins in autumn when atmospheric temperatures drop below zero. The sub-zero temperatures cool the ocean surface of the Arctic basin, driving convective overturning as warmer sub-surface water replaces the already cool surface water (Thomas 2017). The freezing point of seawater is a function of the salinity and density (Thomas 2017). Sea ice will begin to form once the entire ocean surface layer cools to -1.8°C (Wadhams and Davis 2000; Thomas 2017; ESA 2019; NSIDC 2019).

Frazil ice is the earliest form of sea ice, which grows laterally (WMO, 2010; Thomas 2017). Eventually, the frazil ice crystals aggregate to create a highly saline layer of grease ice. In calm conditions, these ice crystals begin to consolidate to a sturdy, but elastic layer of nilas ice (WMO, 2010). Under more turbulent conditions, the ice crystals will solidify by the mechanical action of cyclic compression and decompression, to form pancake ice (Wadhams and David 2000). These pancake ice floes eventually consolidate into solid floes with micro-scale roughness within the surface and bottom topography (Wadhams and David 2000). Thereafter, both ice types are classified based on its thickness. As the ice forms and thickens, the majority of salts (ionic impurities) in sea water are prevented from entering the crystal structure of pure ice and 60-90% of the total volume of salts is rejected (Petrich and Eicken 2010; Thomas 2017). The rejection of salts creates a layer of seawater with high salinity directly below the ocean-ice interface, reducing the freezing point at the ice bottom (Landy *et al.,* 2015; Thomas 2017).

Newly formed sea ice can exhibit micro-scale roughness characteristics due to snow on ice, frost flowers, or turbulent ocean currents. Frost flowers, crystals with dendritic (branching) structures, are formed in calm conditions when atmospheric temperatures and surface wind speeds are low. These crystals grow due to local roughness discontinuities on the surface as the subsurface air layer becomes super-saturated (Style and Worster, 2009; Isleifson *et al.*, 2013).

Sea ice initially achieves its thickness due to thermodynamic processes during the winter growth season. Ice typically grows 1 – 2 metres per growth season (Johannessen *et al.* 2007; Thomas 2017). Thicker ice grows at slower rate than newly formed sea ice and cannot achieve a thickness of greater than 5 m through thermodynamic processes alone (Thomas 2017). In addition to aforementioned thermodynamic processes, the sea ice topography and structure will be modified by dynamic processes. These dynamic processes are result of the mechanical forcing acting upon the surface and bottom of a particular ice floe, which drives deformation of the ice cover. The water and wind drag force are incidentally dependent on the drag coefficient of the surface, which increases as a function of the surface roughness. These phenomena will be further discussed in the following section.

### 2.2.2. Sea Ice Dynamics and Deformation

Ice rheology describes the deformation of ice, which depends on its material properties and acting stress (Hilber, 1979; Leppäranta 2005). Ice rheology is the response to different stresses acting on the sea ice. Ice has near-zero tensile strength, which means if divergent stresses are applied in two dimensions, it will dilate and easily break apart

(Hilber 1979; Williams *et al.* 1993; Hunke and Dukowiez 1997; 2001; Hunke *et al.* 2010). This divergent forcing will cause ice floes to divide and fragment creating open leads, which rapidly freeze over in the winter. Sea ice is easily subject to divergent forcing, as it is a highly fractured material, whilst remaining a largely rigid substance resistant to convergent forcing. Therefore, sea ice has significant shear strength, which implies that when shear stress is applied on ice, it is likely to slip and deform. This shear property facilitates the main cause of rafting and piling up of ice and the formation of rubble, pressure ridges and hummocks under the influence of differential forces at the ice edge (Leppäranta 2005; Hunke *et al.* 2010; Thomas 2017). Deformation, as a result of converging and diverging ice motion can significantly modify the sea ice surface topography (Weiss and Mason 2004).

The three key mechanism of converging deformation are, 1) lateral rafting of thin ice under compression, 2) hummocking of fractured ice blocks in rubble fields, and 3) ridging of ice blocks (Landy *et al.*, 2015). Pressure ridges encompass a sail (ice blocks above sea level) and a keel (ice blocks below sea level), in isotactic equilibrium with respect to sea level, which typically vary between 5 and 30 m (Landy *et al*., 2015; Thomas 2017). Research literature, along with the operational/navigational community, typically use deformed ice and deformation features as notation for ice structures resulting from convergent ice motion, as these ice types generate severe hazards for marine operations and offshore infrastructure (Dierking and Dall, 2007).

The deformation of sea ice is closely related to the motion of sea ice. Sea ice moves as *per* the motion of surface ocean currents at large temporal scales. Local wind forcing causes sea ice motion at small temporal scales. In both cases, the main driving

force is wind forcing (Leppäranta 2005). Diverging/converging wind patterns create diverging/converging sea ice motion, which causes ice deformation. The overall force is expressed by the following equation:

$$F = \tau_a + \tau_w + F_C + F_i + F_t,$$

where $\tau_a$ and $\tau_w$ represent wind and water drag, respectively, $F_c$ refers to the Coriolis force, $F_i$ defines the internal stress of ice mass, $F_t$ refers to the sea surface tilt and $F$ is the total force. The Coriolis effect describes the patterns of deflection taken by objects not firmly connected to the ground as they travel long distances around and above the Earth. The Coriolis force arises due to Earth's rotation. The force equates to zero at the equator and maximizes towards the poles. For example, an ice floe in the northern hemisphere will be deflected to the right of its original trajectory. The sustainability of stress within the ice equates to the strength of the ice cover, which is dependent on the ice thickness and physical properties. Older, thicker ice is typically morphologically more complex and significantly less susceptible to deformation due to its shear mechanical strength (Herzfeld *et al*. 2016).

The thermodynamic and dynamic processes are intrinsically linked, as both processes act together at varying spatial and temporal scales to modify the surface and bottom of the sea ice, hence moderating the ocean-sea ice-atmosphere coupling. Any snow cover present also contributes to the rate of sea ice growth and decay by influencing thermodynamic processes, as well modifying the surface roughness at varying scales. The snow cover also alters the conductive and radiative energy exchange (i.e. the surface albedo) across the ocean-sea ice-atmosphere interface (Baber and Nghiem 1999). This

thesis analyzes surface roughness as a coalescence of the ice surface and the snow cover. Isolating the snow roughness to assess the associated turbulent heat fluxes, and aerodynamic roughness length remains an open area of research (Manes *et al.* 2008). Nevertheless, ice deformation that results in either pressure ridges or leads is the most prominent expression of the morphogenetic complexity of sea ice (Herzfeld *et al*. 2016). As a result, the degree of deformation significantly influences processes acting on the ice cover, in turn being influenced by the same processes. The following sections describe processes which simultaneously affect and are affected by the surface roughness of sea ice: 1) melt ponds, 2) atmospheric drag, and 3) ice thickness.

### 2.2.3. Sea Ice Roughness and Melt Ponds

During the melt season, the surface becomes heterogeneous with the melting of snow and formation of melt water ponds. The depth and geometry of ponds are determined by the local sea ice surface topography, and the volume is determined by the balance of water inflow and outflow. The energy exchanges across the ocean-sea ice-atmosphere interface are poorly understood during the Arctic melt season. Studies have demonstrated that the declining trends in the summer Arctic sea ice is linked to prolonged melt and increasing melt pond coverage (Markus *et al.* 2009; Rösel *et al.* 2012; Schröder *et al.* 2014; Stroeve *et al.* 2014). When these ponds form, the surface albedo drops from >0.7-0.8 to 0.2-0.4, thus increasing the amount of solar radiation which penetrates the ice cover and so becomes available for ice melt (Perovich *et al.* 2002). Projections of sea ice

volume and extent derived from climate models demonstrate a strong sensitivity to variations in the defined albedo (e.g. Curry *et al.* 2001).

Recent sea ice and global climate models have been designed to incorporate melt pond physics into the albedo parameterizations. There has also been extensive effort to create physically based numeric models of pond coverage. However, both rely on melt pond observations and a solid understanding of melt pond formation and evolution, which to date is not well defined. Studies show that seasonal coverage can vary from 25% to 85%, diurnal coverage can vary as much as 35%, and interannual coverage at a single location can vary by 20% (Perovich *et al.,* 2002; Landy *et al.,* 2014; Thomas 2017). The spatial and temporal variability of melt pond formation and evolution is influenced by the history of the mechanical forcing, including, air temperatures, winds, snowfall or any precipitation event, ocean heat flux, ice growth conditions, and ice deformation. Each forcing mechanisms has high spatial and temporal variations. Studies suggest that sea ice topography and its associated roughness acts as major control variable for melt pond coverage (Eicken *et al.,* 2004; Landy *et al.,* 2015). Therefore, deriving regional to basin scale estimates of sea ice roughness presents potential to predict the areal percent coverage of melt ponds.

Smooth, FYI ice typically has larger areal coverage of melt ponds due to low height relief promoting unrestricted flow [Figure 2.1] (Eicken *et al.,* 2004; Landy *et al.,* 2015). Rougher, MYI and deformed ice regions will have restricting bounds on melt pond coverage due to mounds and depressions [Figure 2.1]. Therefore, studies suggest the apparent shift to a larger fraction of FYI, rather than MYI, will contribute to a decrease in summer ice albedo, thus driving a stronger ice-albedo feedback and enhanced

melt, where even less ice persist in the following growth season (Lindsay and Zhang, 2005; Stroeve *et al.*, 2012).

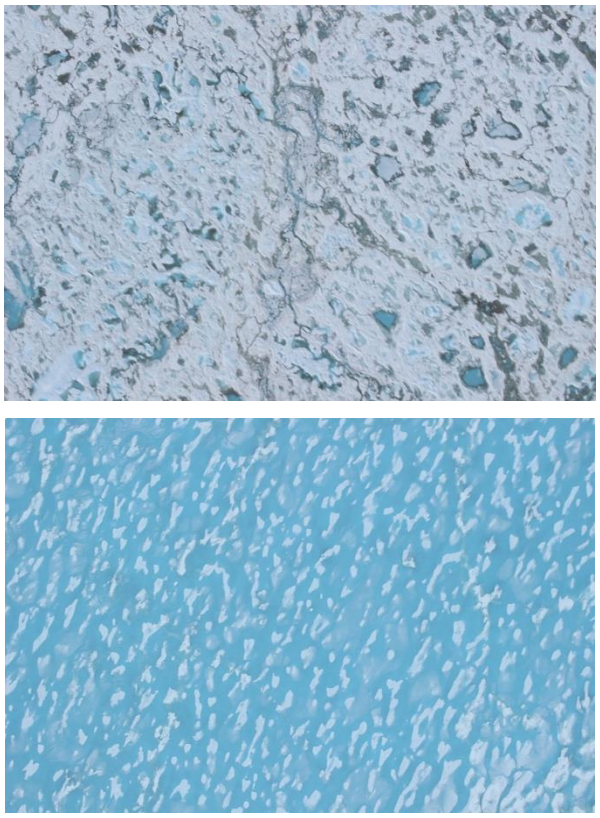

Figure 2.1. Images (~ 640 m x 421 m) from a downward facing camera on an aerial flight in June 2016 displaying the difference in melt pond fraction on different ice types, including more heavily deformed MYI (top) and FYI (bottom).

The relationship between pre-melt (winter) sea ice surface roughness and melt season pond coverage has yet to be fully understood or quantified. As the general imprint of pre-melt surface topography persists throughout the summer melt season, it is assumed that rougher ice will remain rougher compared to smoother ice. Therefore, the mounds and depressions of the surface topography will remain at predetermined locations (Perovich *et al.*, 2012). Few studies have attempted to quantify the relationship between

topography, melt pond fraction, and albedo. However, a recent study conducted by Landy *et al.* (2015) applied quantitative methods to link ice topography derived from satellite images to melt pond fraction. Their results found that 85% of the variance in the summer ice albedo can be explained by the pre-melt sea ice roughness.

### 2.2.4. Sea Ice Roughness and Atmospheric Drag Coefficient

As previously discussed, the sea ice in the Arctic Ocean moves due to the balance of atmospheric, oceanic, and internal forces, i.e. locals winds, ocean currents, and internal ice stress (Castellani *et al.,* 2014). Momentum balance equations describing ice motion, and the intensity of air-ice and water-ice interactions depend on the drag coefficients. The atmosphere-ice (or wind) drag is the dominant component of sea ice momentum balance on seasonal time scales. Above the aerodynamic roughness length (described in Section 2.1), air flow is turbulent and momentum transfer is controlled by the size of turbulent eddies (Thomas 2017). The roughness length of sea ice surfaces ranges from 0.05 to 110 mm (Thomas 2017).

Spatial and temporal variations of the sea ice surface topography will provoke spatial and temporal fluctuations in drag coefficients. Pressure ridges increase the inertia of drifting ice and the effective roughness of the upper and lower surfaces of the sea ice. Understanding the dynamic coupling between the ice, ocean, and atmosphere requires a detailed representation of these momentum fluxes (Castellani *et al.,* 2014). In current work, the ocean-sea ice-atmosphere system is studied by investigating how numerical simulations are affected by sea ice surface roughness. Recent studies have developed parameterizations using topographic data that describes the dependence of the drag

coefficients on pressure ridges, floe distribution, melt ponds, and on the keel distribution (e.g. Petty *et al.* 2017). As remote sensing technology has the ability to obtain real-time and large-scale sea ice information, there is ongoing research to retrieve parameters describing the atmospheric drag coefficient from satellite-based remote sensing, in particular SAR backscatter. As SAR backscattering is related to the physical roughness of the surface, a relationship must first be investigated between the aerodynamic roughness lengths to physical sea ice roughness.

### 2.2.5. Sea Ice Roughness and Ice Thickness

Similar to topography, the thickness distribution of sea ice is dependent on the formation and evolution of the ice floe (Landy *et al.*, 2015). Studies have shown a promising link between sea ice thickness and sea ice roughness, as the thickest ice in the Arctic region consists of heavily deformed ice, with high surface height deviations (Thomas 2017). Deformed ice consists of both FYI and MYI, which has been subject to atmospheric and oceanic pressure, forcing ice upwards and downwards from the surface (Thomas 2017). Thick MYI ice and deformed ice features impose severe restrictions on shipping traffic due to their greater thickness (Johannessen *et al.* 2017). Extreme ice features formed by deformation processes encompass a large portion of the sea ice volume and are often indistinguishable between other ice types. The detection and classification of these extreme ice features is imperative to enhance our understanding of sea ice dynamics and to improve hazard mapping in the Arctic region.

## 2.3. Remote Sensing of Sea Ice Surface Roughness

Surface roughness is generally treated as a stationary, single-scale random process, describing height deviations from a reference level. Pragmatically, natural surfaces are characterized by an aggregate of several superimposed scales of roughness. Therefore, what constitutes as "rough" or "smooth" depends on the application and features of interest (i.e. scale). Measurements of sea ice surface roughness have been performed over the recent decades on different scales and using various techniques and instruments (Paterson *et al.* 1991; von Saldern *et al.* 2004; Gupta *et al.* 2012; Landy *et al.* 2015; Beckers *et al.* 2015). Manninen (1997) provided an extensive study on the fractal nature of sea ice surface roughness, however, the definition of sea ice surface roughness has shifted to reflect how instruments are utilized to define and describe the sea ice topography. A number of instruments are used to observe and monitor changes in the sea ice cover and dynamics, including laser altimeters, sonars, aerial and terrestrial LiDAR, optical satellite data, microwave remote sensors and more recently, interferometric synthetic aperture radar (InSAR). However, due to the spatial variability and multiscalar nature of roughness, instruments with different measuring ranges yield parameter values that are not easily compared. Although terrestrial and airborne data provide fine-scale data, it is not feasible to derive regional-scale measurements. These instruments however can be used to interpret and validate the coarser satellite-borne data. The advantage of a satellite-based roughness retrieval is that it provides larger coverage and could enable surface change detection mapping between seasons.

Passive and active microwave remote sensing systems are particularly well suited for the Arctic as the long microwave wavelengths (0.3-300Ghz; 300-1mm) penetrate

clouds and detect the surface in all weather conditions and without sunlight. Passive sensors, termed radiometers, detect microwave radiation that is naturally emitted or reflected from the Earth's surface. Due to the low energy content of long wavelength (low frequency) microwaves, the energy available is quite small and therefore requires a large field of view to detect the energy. This often limits most passive sensors to very low spatial resolutions. However, the low spatial resolution often enables a larger areal coverage, which has been crucial in Arctic-wide mapping of sea ice concentrations. Conversely, active remote sensing systems are not dependent on the Sun's electromagnetic (EM) radiation or the thermal properties of the Earth, as they provide their own energy source of illumination. The system employs a transmitting and receiving antenna. The transmitter emits radiation that is directed towards a target and the receiver senses radiation backscattered from the target. The advantage of active sensors is the power to detect a surface anytime, regardless of the time of day or season, as well as the ability to examine wavelengths that are not sufficiently provided by the sun and to better control the illumination of a specific target (Ulaby *et a.* 1984; Richards 2009; Natural Resource Canada 2019; ESA 2019). Active sensors can also achieve a much higher spatial resolution (described below).

The most commonly used active remote sensing systems is radar (Radio Detection and Ranging), which utilizes the longer wavelength microwaves (3-25 cm). When RADAR systems were first developing in the late 1800s and early 1900s, they targeted the relatively long radio waves, and were used for aircraft and ship detection. The first imaging radars appeared during the Second World War and shortly after, side-looking airborne radars (SLAR) were developed for military terrain surveillance. In the

1950s and 1960s, advances in SLAR led to the development of synthetic aperture radar (SAR). The resolution from a real-aperture radar is limited by the length of its antenna; for this reason SAR was developed. SAR synthesizes a very long antenna by exploiting the forward motion of a platform carrying a relatively short antenna to successive positions along the flight line. The successive positions are processed as individual elements of the same antenna, thus achieving a higher resolution (Richards 2009; Natural Resource Canada, 2019; ESA 2019). The increased spatial resolution at the expense of a smaller swath, in comparison to other microwave sensors, enables observations of regional and local variations of sea ice parameters (Dierking, 2013). Recently launched polarimetric SARs (pol-SARs) can discern resolution cells under 10 m.

The physical basis of microwave remote sensing of sea ice lies in how microwaves interact with the sea ice surface and structure. To retrieve geophysical properties from an image, a link must first be drawn between physical measurements and image values. The magnitude and intensity of the backscattered energy depends on the properties of the detected feature (i.e. target parameters), as well as characteristics of the transmitted energy (i.e. sensor parameters). It is crucial to understand how characteristics of both the target and the sensor system influence the backscattering signal retrieved, in order to determine the optimum combination of parameters to be used. Target parameters of the sea ice cover include the orientation of the ice features, dielectric properties, environmental conditions, and the local incidence angle. Sensor parameters include the polarization, frequency, resolution, and sensor incidence angle. Although some of these parameters are inherently linked and their individual influence cannot be easily isolated, research has demonstrated consistent relationships between various parameters and

microwave backscatter. Studies have shown that microwave sensors are most sensitive to the roughness of the reflecting surface on scales of the radar wavelength, changes in the local incidence angle of the radar beam on scales larger than the radar wavelength, inhomogeneities such as cracks and air bubbles in the ice volume, and the dielectric properties of ice (Dierking and Dall, 2007; Dierking 2013; Richards 2009; Shokr and Sinha 2015)

Estimating surface roughness by means of SAR remote sensing methods remains a major challenge. Changes occurring in the ice surface signatures at much smaller temporal and spatial scales than provided by the satellite's incoming EM waves can be reflected from the surface or from the volume of rough ice. To study the roughness of the sea ice surface, it is important to understand the EM wave scattering mechanisms from sea ice. The following texts will briefly discuss the interactions between microwave energy and the sea ice cover. First, this section will provide a discussion on how the dielectric properties of sea ice, along with its internal structure and surface geometry, influence how the EM energy scatters. The following section will consider how different components of the SAR system (i.e. polarization, frequency, incidence angle, resolution) can also influence the interactions between the EM energy and the sea ice surface.

An incident EM wave upon the surface of a medium can be scattered by dielectric discontinuities at the surface or transmitted across the boundary into the medium (Richards 2009; Shokr and Sinha 2015). Within the medium, the wave can continue through the medium or be scattered by dielectric discontinuities in the medium. Scattering which takes place at the interface of two media is referred to as the surface scattering, whereas scattering which occurs within a medium is known as volumetric

scattering. The relative contribution of the two scattering mechanisms is a function of the relative permittivity of the iced-covered region, which describes the electrical properties of the material. The relative permittivity is denoted as,

$$\varepsilon = \varepsilon' + i\varepsilon'',$$

where the real part describes the relative constant, which defines how easily an incident microwave can pass through a dielectric interface and the imaginary component describes the effective relative dielectric loss of the material. The relative permittivity of sea ice is mainly dependent on the microwave frequency, sea ice salinity, and temperature. The relationship between the real and imaginary components also controls the penetration capability of the incoming microwave (Carsey 1992; Richards 2009; Shokr and Sinha 2015; Thomas 2017).

The complex dielectric constant of a surface is a measure of the electric properties, consisting of two parts, the aforementioned permittivity and the conductivity, that are both highly dependent on the moisture content and the material considered. A change in moisture content generally provokes a significant change in the dielectric properties of a natural material; increasing moisture is associated with increased radar reflectivity. The electromagnetic wave penetration in a medium is an inverse function of water content. Currently, the most perplexing conditions to observe sea ice occur during the melting season in the late spring and summer months. The presence of water on the ice surface (FYI or MYI) inhibits EM waves at higher frequencies to detect the ice surface, as they cannot penetrate through the melt layer. Therefore, surface scattering dominates during the melting season.

During dry conditions prior to the onset of melt, surface scattering is often the dominant scattering mechanism over FYI, which is highly saline and therefore has a high dielectric constant. This means little transmission of EM energy passes into the ice, resulting in minimal or no volumetric scattering. If FYI is rough, the surface scattering is enhanced due to increased surface geometry. While FYI primarily scatters EM radiation from the surface due to its high salinity levels, volume scattering is observed in MYI due to its low salinity and the presence of air bubbles in the space once occupied by brine pockets. The EM wave can easily penetrate deeper into MYI. At higher frequencies, there is increased volume scattering as the air bubbles become comparatively larger than the wavelength. The surface roughness of MYI also contributes significantly to the backscattering for higher frequencies (e.g. X, Ku band) (Richards 2009; Shokr and Sinha 2015).

In terms of SAR remote sensing, roughness is a relative concept depending upon the wavelength and the incidence angle. From a scattering physics perspective, a surface is held to be "rough" if its structural properties have dimensions that are comparable to the incident wavelength. According to the Rayleigh criterion, a surface is considered smooth if

$$h < \frac{\lambda}{8 * \cos\theta}$$

and considered rough if:

$$h > \frac{\lambda}{8 * \cos\theta}$$

where $h$ refers to the mean height of surface variations, λ refers to the wavelength, and θ denotes the incidence angle. The Rayleigh criterion describes the threshold at which a

surface becomes rough enough to backscatter. In the case of pure surface scattering, as the surface becomes rougher, the amount of backscatter increases. The following section will discuss how wavelength and incidence influence the backscattered energy detected from sea ice, as well as, the impact of polarization channels and ratios.

### 2.3.1. SAR System Parameters

#### *A) Wavelength*

Within the microwave portion of the electromagnetic spectrum, there are only a number of bands that have been used for radar imaging. The most commonly used frequency bands for SAR systems are listed below in Table 2.1. The X-, C-, and L-band have advantages in terms of sea ice surveillance and research. Details regarding historical and current satellites using these bands are presented in Table 2.2, along with their utility when observing the sea ice environment. In addition, experimental ground and airborne radars using the Ku- and P-band have been used in the sea ice environment. In 2021, the European Space Agency (ESA) is set to launch a fully polarimetric P-band SAR satellite. The P-band has very significant penetration capabilities with regard to vegetation canopies, glacier, and sea ice (Richards 2009; Dierking 2013; ESA 2019; Natural Resource Canada 2019).

The frequency of the incident radiation determines the penetration depth of the waves into a medium and the relative roughness of the surface considered. More penetration in a medium will occur as the wavelength increases, generating a larger volumetric contribution in the backscattered signal. As previously mentioned, it should be noted that penetration capabilities are also related to the moisture content of the target.

The choice of frequency band is particularly important when observing and estimating sea ice surface roughness as the sea ice surface is imbedded with various scales of roughness features. The incoming radiation is sensitive to target features half the size of the wavelength or larger (Richards 2009; Dierking 2013). At smaller wavelengths, a concentration of smaller roughness features imbedded within larger features may yield high backscatter intensity, as discussed below.

This thesis uses only C-band and L-band to assess the utility of SAR to estimate sea ice surface roughness. C-band frequency penetration into winter FYI is negligible. In this case, backscatter occurs primarily from the brine-wetted snow-ice interface, and increased roughness (e.g. small-scale roughness, ice fragments, ridge blocks) leads to increased backscatter (Ulaby *et al.* 1986; Dierking and Dall 2007). Backscatter intensity is strongly dependent on the wavelength scale surface roughness, therefore influences from microscale features (i.e. millimetres to centimetre scale surface roughness for FYI, air bubbles in MYI) are large enough for significant intensity changes at C-band (Eriksson *et al.* 2010). At L-band frequency, the penetration depth in FYI is on the order of centimetres and the wavelength is considerably larger than the small-scale roughness (mm to cm) and the brine inclusions (or air bubbles in MYI) in the ice volume. Therefore, the intensity level of undeformed ice in the SAR imagery is much lower at L-band. L-band also penetrates deep into the low-salinity ice and is much more sensitive to larger (cm to m) irregularities in the ice structure (e.g. deformation processes) or can even interact with the ice-water interface (Dierking and Busche 2006).

Table 2.1. Radar frequency bands with their defined frequency and wavelength ranges.

| **Frequency Band** | Ka | Ku | X | C | S | L | P |
|---|---|---|---|---|---|---|---|
| **Frequency [GHz]** | 40-25 | 17.6-12 | 12-7.5 | 7.5-3.75 | 3.75-2 | 2-1 | 0.5-0.25 |
| **Wavelength (cm)** | 0.75-1.2 | 1.7-2.5 | 2.5-4 | 4-8 | 8-15 | 15-30 | 60-120 |

Table 2.2. Current and past satellites of the most commonly used bands in sea ice monitoring and their utility and advantage (Dierking and Busche 2006; Dierking 2013; Johannessen *et al.* 2016; Singha *et al.* 2018).

| **Wavelength** | **Current and Past Satellites** | **Utility and Advantages** |
|---|---|---|
| **X** | SAR-Lupe (2008-Present)<br>Cosmo-SkyMed (2007-Present)<br>TerraSAR-X (2007-Present)<br>TanDEM-X (2010-Present)<br>KOMPSAT-5 (2013-Present)<br>PAZ (2018-Present)<br>Cosmo-SkyMed SG (2019-Present) | • Strong sensitivity to the ice surface<br>• Separation between newly forced sea ice and open water<br>• High spatial resolution<br>• Lead detection |
| **C** | ERS-1 (1991-2000)<br>ERS-2 (1995-2011)<br>Radarsat-1 (1995-2013)<br>Envisat (2002-2012)<br>Radarsat-2 (2007-Present)<br>Risat-1 (2012-2017)<br>Sentinel-1a (2014-Present)<br>Sentinel-1b (2016-Present)<br>RCM (Launch date: 2019) | • Better separation of MYI ice from FYI ice<br>• Sensitive to ice thickness<br>• Long records of C-band SAR |
| **L** | JERS (1992-1998)<br>ALOS (2008-2011)<br>ALOS-2 (2014-Present)<br>SOACOM-1a (2018-Present)<br>SOACOM-1b (Launch date: 2019)<br>NISAR (Launch date: 2019) | • Better discrimination of ice types during the melting period<br>• Better delineation of deformation features (i.e. ridges) from smooth ice areas.<br>• Less affected by small-scale roughness<br>• Strongly influenced by deeper portions of the ice<br>• Lead detection |

### *B) Polarization*

Radar polarisation is the orientation of the electric field in an electromagnetic wave, which is orthogonal to the magnetic field. Conventional polarimetric SARs are usually designed to transmit and receive waves that are linearly polarized on vertical (V)

or horizontal (H) planes. This means the SAR is capable of recording amplitude and phase information of backscattered energy for four transmit-receive polarizations (HH, HV, VH, and VV). When the polarisation of the received is the same as the transmitted radiations, this is called like-polarization. Whereas, when the polarisation of the received is the opposite of the transmitted, this is called cross-polarization. The backscattered energy from a target is dependent on the relationship between polarisation state and the physical structure of the target. Polarimetric ratios are simply power ratios of backscattered energy (i.e. HV/HH or HH/VV). Polarization ratios have utility in reducing the ambiguity caused by the non-linearity between system response and target properties. However, the possible states of polarization include all angular orientations of the electric vector, leading to elliptical and circular polarization (Richards 2009; Dierking 2013; Natural Resource Canada 2019). These polarisation states are not researched in this thesis, however, their utility in the sea ice marine environment has become increasingly appealing due the launch of Canada's RADARSAT Constellation Mission (RCM) in June 2019.

Findings assessing the polarization response, particularly of FYI, vary. Melling (1998) described the advantage of using HH over VV for contrasting between level and deformed ice. Higher contrast can be explained by a lower backscatter response from smooth ice at HH and a weak dependence on the direction of polarization from deformed ice (Manninen 1992; Melling 1998). In later studies, the HV channel was found to provide the largest contrast between level and deformed FYI (Mäkynen *et al.* 2002; Dierking and Dall 2007; Gegiuc *et al.* 2018). Unfortunately, HV backscatter from level FYI can be very close to the SAR noise floor. The copolarized channels remain the most

assessible and reliable and, according to Deirking and Dall (2007), either HH or VV channels at L-band are preferred over C-band for deformation mapping. Conversely, the cross-polarization ratio acts as an estimate of depolarization and is expected to increase with increasing roughness (Gill and Yackel 2012; Gill *et al.* 2013; Moen 2013; Hossain *et al.* 2014; Fors *et al.* 2016).

### *C) Incidence Angle*

The backscatter of the surface (i.e. the sea ice surface) will likely have angular dependence based on the incoming wave. The incidence angle defines the angle of the incident radar beam and the vertical normal to the target surface. Changes in the incidence angle will affect the radar backscatter from a surface or target. Typically, the backscatter intensity decreases with increasing incidence angle. Incidence angle also influences the relative contributions of surface and volume scattering. Backscatter from surface scatterers is often strong at steep incidence angle and decreases at shallower incidence angles. The rate of decrease slows when imaging a rougher surface as a rough surface creates a more variable and random backscatter. The intensity of volumetric scattering is less dependent on incidence angle (Richards 2009; Natural Resource Canada 2019).

Surface scattering is dominant at incidence angles less than 45 degrees, and volume scattering from FYI at C-band is recognisable only at shallow incidence angles (Carlstrom and Ulander 1995; Dierking 1999). There are a few studies assessing incidence angle influences on sea ice backscatter measured at L-band SAR. Casey *et al.* (2016) found that the contrast between FYI and MYI is small and nearly disappears at

small incidence angles, though Dierking and Dall (2007) note that the contrast between level and deformed ice is maintained across all incidence angles at L-band. Recently, Mahmud *et al.* (2018) investigated incidence angle dependence from HH backscatter over FYI and MYI at L-band and C-band SAR. Incidence angle dependence over FYI was similar at C-band and L-band, whereas MYI dependence doubled at L-band compared to C-band. Mahmud *et al.* (2018) concluded that incidence angle dependence is much more evident at L-band.

The physical surface roughness of sea ice is complex to understand, and equally difficult to measure, estimate, and parameterize using surface-based and remote sensing techniques. Satellite data opens the pathway to acquiring comprehensive datasets in the CAA and the surrounding Arctic environment. The following chapter includes work using airborne and satellite data for understanding surface roughness in the CAA, and for making satellite-based estimations of sea ice roughness.

# Chapter 3 : Estimation of level and deformed winter first-year sea ice surface roughness in the Canadian Arctic Archipelago from C- and L-band synthetic aperture radar

## 3.1. Introduction

Traditional synthetic aperture radar (SAR) technology (i.e. non-interferometric SAR) has been used extensively to monitor and quantify physical characteristics of sea ice in the Arctic due to its all weather, day/night, and cloud penetrating imaging capabilities. Its predominant sensitivity to surface roughness has prompted considerable interest in exploiting SAR to generate surface roughness maps of various geographical regions and surface types. Studies have successfully used SAR to determine roughness characteristics of agricultural lands, flood plains, and arid environments (Martinez-Agirre *et al.* 2017; Sadeh *et al.* 2018).

Sea ice during cold conditions is a heterogeneous mixture of ice crystals, air pockets, and liquid brine (Hallikainen *et al.*1986). The relative fractions of these constituents influence the complex permittivity which, along with the sea ice roughness and other surface and volume properties, determines the intensity of backscatter that returns to the receiver. SAR backscatter is primarily controlled by surface roughness variations smaller than the microwave wavelength (Richards 2009; Paterson *et al.* 1991). For higher frequency sensors, the sea ice surface features often exceed the wavelength, having larger, macro-scale variations, which also strongly influence SAR backscatter (Richards 2009). Relationships between backscatter and sea ice surface roughness are complicated by contributions from the ice volume and geometry of dielectric discontinuities such as brine inclusions in FYI, and air bubbles in freshened MYI. In the

melting season, large portions of the sea ice surface are masked due to the presence of melt ponds, which are manifested in the low backscatter intensity. Utilizing SAR for deriving sea ice geophysical variables remains an active area of research due to the complexity of surface roughness and dielectric properties affecting SAR backscatter. In addition to the surface conditions and volumetric discontinuities, backscatter is also a function of the properties of the transmitted energy (i.e. frequency, incidence angle, polarization).

C-band (4-8 GHz frequency; 3.8-7.5cm wavelength) is the most commonly used frequency as it is considered a compromise for all-season sea ice monitoring in operational ice charting activities. Numerous studies have related C-band SAR scenes with sea ice surface roughness measurements from airborne laser altimeters, ground-based laser systems, and airborne laser scanners (e.g. Dierking and Carlstrom 1997; Melling *et al.* 1998; Peterson *et al.* 2008; Gupta *et al.* 2013; Fors *et al.* 2016). Earlier studies focused primarily on the contrast in roughness and associated backscatter between level floes and large-scale deformation features, such as ridges. It was found that extensive areas of small-scale deformations with lengths scales only a few radar wavelengths are strong enough to affect the radar return of the embedded features (Dierking *et al.* 1997; Melling 1998). This suggests that longer wavelengths are preferred when detecting larger deformation features. Longer wavelengths also have potential to improve imaging during the melt season due to increased penetration depth. Availability of imagery from the ALOS Phased Array type L-band SAR 2 (PALSAR-2), (operational since 2014) has attracted renewed interest in assessing backscatter signatures from sea ice at L-band (1-2 GHz; 15-30cm).

Since the establishment of SAR, more sensors operating at C-band has led to more sea ice property studies focused on that frequency. A number of studies (e.g. Carlstrom and Ulander 1995, Peterson *et al.* 2008, Similä *et al.* 2010) have observed good agreement between C-band SAR backscatter and independently quantified measurements of the physical roughness of the sea ice surface, where an increase in surface roughness has led to an increase in backscatter. However, since backscatter is not exclusively related to the physical roughness of the surface, high backscatter can be attributed to other sea ice properties. For example, high backscatter has also been detected from leads with very low surface roughness (Peterson *et al.* 2008). This was a result of frost flowers causing small-scale surface roughness combined with high dielectric contributions to the C-band backscatter. In another case, von Saldern *et al.* (2004) observed very high backscatter from areas of multiyear level ice with sparse ridges and an overall low surface roughness root-mean-square (rms). Volume scattering from MYI was likely the dominant scattering mechanism, generating high levels of backscatter. Similä *et al.* (2010) compared C-band SAR backscatter with surface roughness measurements from a 3-D laser scanner in the Baltic Sea and found good agreement between model predictions and measured values. However, their results confirmed that the ability to use C-band is severely compromised if backscatter originates from MYI. More recently, Fors *et al.* (2016) compared altimeter-derived sea ice roughness rms measurements to polarimetric SAR features, along with backscatter coefficients. They found good agreement with various polarimetric features, however, the correlation scores between rms and backscatter coefficients were comparable to those of the highest scoring polarimetric SAR features, especially in the smoother sections.

In this chapter, the utility of C-band and L-band SAR for mapping sea ice surface roughness is assessed using late winter period observations of cm-scale vertical variations in the physical roughness derived from airborne laser scanner measurements. Two questions are investigated: 1) what is the relationship between winter measured FYI surface roughness, and C- and L-band frequency backscatter?; and 2) how are relationships between FYI surface roughness, and C- and L-band frequency backscatter, affected by advanced melt? The first question is motivated by the need to develop SAR-based maps of sea ice surface roughness. The second question provides a useful means for assessing the drivers of C- and L-band backscatter during advanced melt (in particular the understudied L-band frequency), and for further establishing the utility of SAR imagery acquired during melting conditions to understand sea ice deformation, and by proxy sea ice strength and mass balance, in scientific and operational contexts.

## 3.2. Data and Methods

### 3.2.1. Study Area

This study investigates a landfast ice region found in Victoria Strait within the Canadian Arctic Archipelago (CAA) [Figure 3.1]. Landfast ice refers to sea ice that is attached to the shoreline with little or no motion, in contrast to pack ice which drifts around the sea (WMO 1970). After freeze-up and until break-up, the sea ice is not heavily influenced by wind driven movement due to its land-locked nature (Melling 2002). The ice found within Victoria Strait is a combination of ice formed *in situ* and older ice floes that have been advected into the region from elsewhere, resulting in thick FYI and older multi-year ice floes which, according to airborne snow plus ice thickness

measurements made in April 2011 and 2015, have an average thickness around 2.51 m (Haas and Howell 2015). In April/May, the snow thickness in the CAA ranges between 0.2 m and 0.4 m (Brown and Cote 1992; Melling 2002; Haas and Howell 2015).

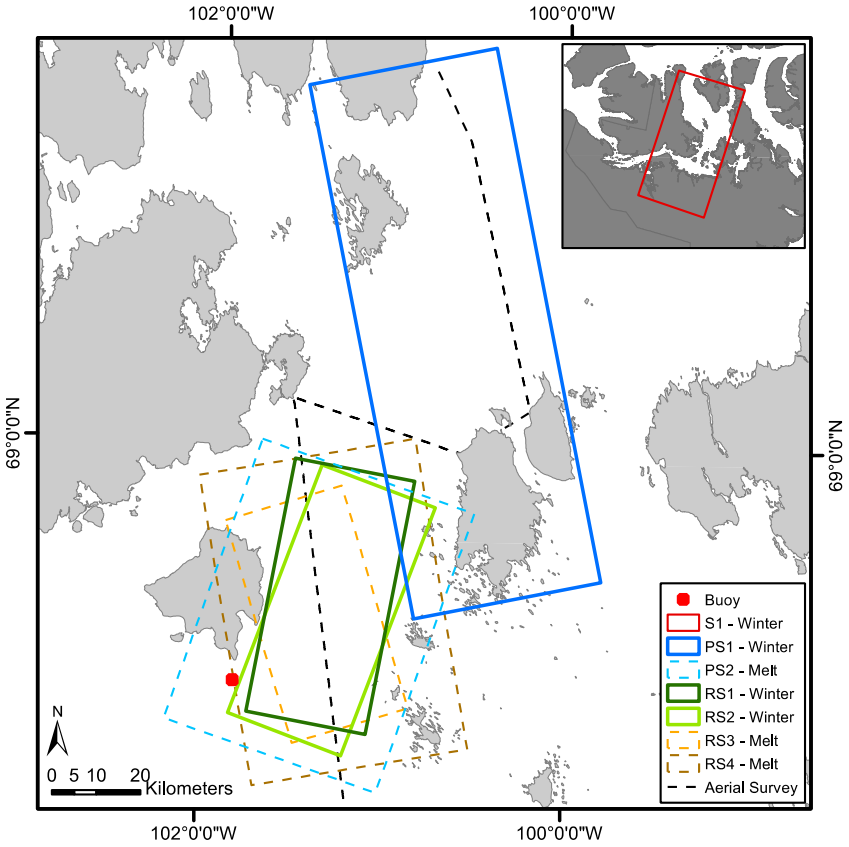


Figure 3.1. Geographic map of study area showing image footprints, aerial survey and buoy locations.

The immobile nature of the landfast ice in this region is ideal for studying sea ice evolution because there is negligible ice drift between acquisition times of the SAR imagery in the winter and melting conditions (Barber *et al.,* 1992; Nasonova *et al.* 2017). Due to the land locked nature of landfast ice, sea ice conditions in the late winter period representing the seasonal maximum in ice growth can be surveyed (e.g. Haas and Howell 2015) and the evolution of the same ice can be studied through melting stages and up to

break-up without having to track ice movement. This approach was used in this study, as described in the next section.

### 3.2.2. Data Collection

Primary data for this study were collected during the winter (pre-melt) period from March through April 2016. Three high-resolution SAR scenes in C- and L-band frequencies were collected for examining roughness and backscatter relationships. Three additional RADARSAT-2 and PALSAR-2 images, acquired in June 2016 and spatially coincident to the winter scenes, were also acquired to investigate the influence of melt on roughness and backscatter relationships. An airborne survey of ice roughness and thickness was carried out on April 8th, 2016 and an airborne aerial photography survey was conducted on June 23rd, 2016 along the same track as the winter-period survey The locations of SAR image footprints and aerial survey track are shown above Figure 3.1, with details of the collected SAR images shown in Table 3.1 and further described below.

Table 3.1. Image properties and acquisition details. Incidence angle is defined by the angle at the scene centre. Resolution is given in azimuth and range.

| Scene ID | Date (mm/dd/yyyy) | Time (UTC) | Instrument | Incidence Angle (°) | Resolution (m) | Nominal NESZ (dB) | Season |
|---|---|---|---|---|---|---|---|
| PS1 | 03/16/2016 | 06:15 | ALOS2/PALSAR-2 | 28 | 3.1 x 3.1 | ≤ -36 [1] | Winter |
| S1 | 04/09/2016 | 13:34 | Sentinel-1 | 35 | 20.0 x 40.0 | ≤ -22 [2] | Winter |
| RS1 | 04/24/2016 | 13:04 | RADARSAT-2 | 45 | 13.5 x 7.6 | ≤ -37 [3] | Winter |
| RS2 | 04/26/2016 | 13:46 | RADARSAT-2 | 22 | 13.5 x 7.6 | ≤ -37 [3] | Winter |
| RS3 | 06/23/2016 | 23:47 | RADARSAT-2 | 23 | 13.5 x 7.6 | ≤ -37 [3] | Melt |
| RS4 | 06/23/2016 | 00:17 | RADARSAT-2 | 41 | 13.5 x 7.6 | ≤ -37 [3] | Melt |
| PS2 | 06/23/2016 | 19:36 | ALOS2/PALSAR-2 | 38 | 3.1 x 3.1 | ≤ -36 [1] | Melt |

[1] JAXA, 2008; [2]ESA, 2012; [3]CSA, 2011

Between April 27th, 2015 and July 19th, 2015, surface air temperature at 0.5 m height and 0.1-degree accuracy was recorded using an Oceanetic *IceTemp Profiler* located in FYI in the southwest portion of the study area. These data are shown in Figure 3.2, along with air temperature data from the nearest Environment Canada station (Cambridge Bay) leading up to the period when the buoy was operational.

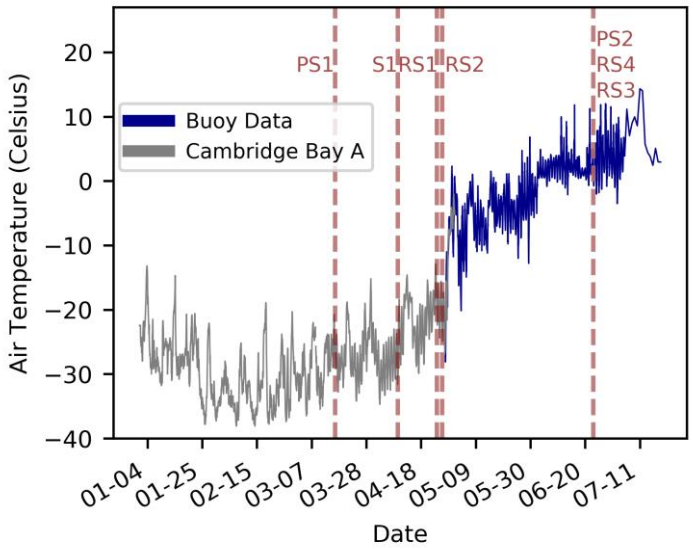


Figure 3.2. Air temperature evolution plot with measurements from the Environment Canada station Cambridge Bay (grey) from January 1st to April 30th and measurements derived from the buoy data south of Jenny Lind Island (dark blue), from April 27th to July 1.

### *A) SAR imagery*

SAR data include Fine Quad Polarimetric scenes from the Canadian RADARSAT-2 satellite (5.405 GHz, wavelength 5.5 cm) and High Sensitive Quad Polarimetric scenes from JAXA ALOS-2 PALSAR-2 satellite (1.270 GHz, 23.6cm) (CSA 2011; JAXA 2008) [Table 3.1]. In Victoria Strait, four spatially coincident RADARSAT-2 images were collected: two acquired in April 2016 at scene-centre incidence angles ($\theta$) of 45° and 22° and two corresponding spring scenes acquired in June

2016 at incidence angles of 41° and 23°. A PALSAR-2 image that overlaps the RADARSAT-2 dataset was acquired in June 2016 ($\theta$=38°); however, the only winter PALSAR-2 scene acquired in March 2016 ($\theta$ =28°) was positioned to the northeast of the RADARSAT-2 images, though still covering the survey track [see Figure 3.1] and was comprised of a similar ice regime. All images cover regions of thick FYI and MYI ice, however, a larger concentration of MYI is found throughout the winter PALSAR-2 (PS1) scene due to its more northern location. The portion of the aerial survey track utilized in this study only covered areas of FYI.

For consistency, all SAR images were radiometrically calibrated to sigma-nought and a Lee speckle filter with a 7 x 7 window was applied to reduce image speckle and retain detailed signal information (Lee 1986). The images were resampled to a 20 m pixel spacing as a compromise between sensors, and with the aim of extending the results to other SAR imaging modes with similar pixel spacing and much larger swath coverage. The images were map projected to the UTM/WGS-84 projection. The beam mode for ALOS-2 PALSAR-2 images has a geometric accuracy of 6.94 m and the beam mode for the RADARSAT-2 images has a geometric accuracy of <10 m.

Backscatter bands of all four transmit-receive polarization combinations (HH, HV, VH, VV) were used, and polarimetric ratios, *co-polarization* ($R_{VV/HH}$) and *cross-polarization* ($R_{HV/HH}$) were derived.

### *B) Airborne Surface Roughness and Thickness Survey*

Late-winter surface roughness and thickness were observed with an airborne sensor package operated from a DC3/Basler BT67 aircraft flown on April 8$^{th}$, 2016. This

survey captured late winter conditions at the time of maximum sea ice thickness when it is assumed that little subsequent surface variability will occur until melt onset (Nasonova *et al.* 2017). Surface roughness was derived from a Riegl LMS Q120 near-infrared laser scanner mounted at the bottom of the fuselage of the aircraft. With a nadir field of view of 80° perpendicular to the flying direction, and a flying altitude of 100 m, every scan line was approximately 120 m wide across-track, with 200 measurements at an angular resolution of 4°. The scan rate was 50 lines per second with a speed of 120 knots, resulting in a scan line spacing of approximately 1.2 m along the flight track. The accuracy of the individual range measurements is 25 mm, with a precision of 15 mm (Beckers *et al.* 2015). Surface roughness was retrieved following the method described by Beckers *et al.* (2015). Each scan line was fitted with a flat-earth hyperbolic function and surface roughness was calculated from each scan line as the standard deviation of the difference between measured and fitted flat-earth surfaces. The obtained surface roughness measurements therefore corresponds to the root-mean-square roughness ($s_{rms}$). The rms is one of the most common parameters used to describe surface roughness.

It is important to note that the $s_{rms}$ obtained thus represents surface roughness in general as the ice is typically covered by snow in late winter. The 2D laser scanner used to measure surface roughness cannot effectively penetrate through snow, therefore the returned $s_{rms}$ is a consequence of the combined snow and ice topography. This can lead to an underestimation of the ice surface roughness of DFYI due to accumulated snow in depressions, as well as misrepresentation of level ice due to the roughness of snow.

In addition to the roughness measurements, ice thickness was observed by means of electromagnetic induction (EM) sounding using a sensor towed by the aircraft (EM

Bird; Haas *et al.* 2009; Haas *et al.* 2010; Haas and Howell, 2015). The ice thickness distributions were mostly used as a supporting dataset to understand and interpret the targeted ice structure. In addition, the relationship between surface roughness and thickness was investigated.

### *C) Aerial Photography*

An airborne Twin Otter aerial photography survey was conducted on June 23rd, 2016 along the same track as the winter-period DC3 survey. A total of 1069 downward-looking digital true-color aerial photographs were acquired with image dimensions of 630 +/- 40 m by 421 +/- 27 m, and a pixel spacing of 0.12 +/- 0.01 m (variations are due to changes in the aircraft altitude). Aerial photos were classified into ice and water, for the purpose of estimating melt pond fraction. This was achieved using a semiautomatic technique whereby thresholds were applied to the images to classify the image pixel by pixel, which created three classes: open water (mostly cracks), melt, and ice [Figure 3.3]. However, as the study area was over fast ice there were only 5 images within the open water class representing open cracks, and these were not within the study area.

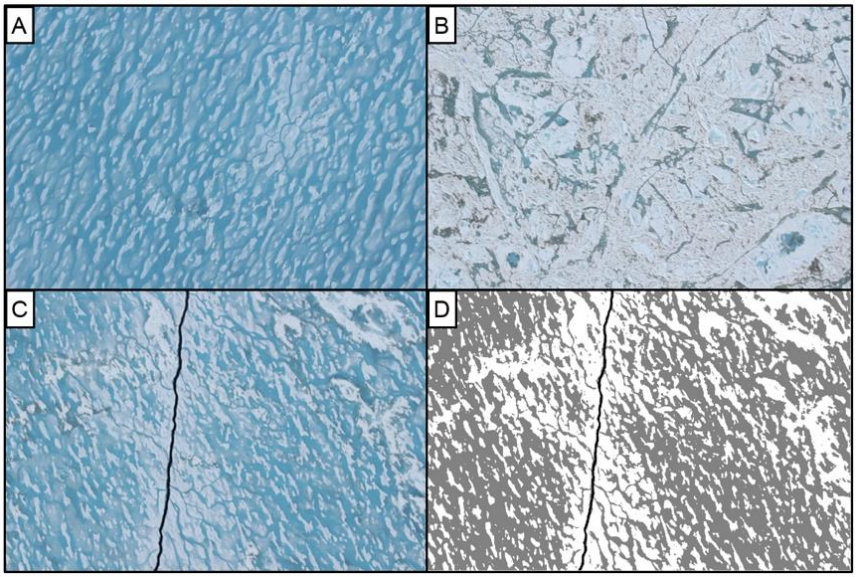


Figure 3.3. Examples raw images and a classified image from the June 2016 aerial survey imaging melt pond fraction; [A] surface flooded with melt ponds over FYI region ($f_p$=0.76), [B] scattered melt ponds in DFYI region ($f_p$=0.12), [C] sea ice with lead prior to classification, [D] classified image of image in [C]. White portions show ice concentrations, grey regions represent melt water, and black regions represent open ocean water.

The photos were used as detailed visual reference for the assessment of the stage of melt and interpretation of backscatter signatures of temporally coincident SAR images. The photographs show evidence of significant melt pond coverage, with more melt ponds generally associated with smooth ice areas [Figure 3.3]. Together with the air temperature record, it was determined that the sea ice was in an advanced melt stage, having consistently above freezing air temperatures since June 2$^{nd}$, 2016. A cursory examination of satellite MODIS instrument data revealed that melt ponds formed in the region on approximately June 7$^{th}$, 2016. Given the extent of melt prior to the June SAR image acquisitions, there was very likely negligible to no snow remaining on the sea ice.

### 3.2.3. Data Analysis

As a means to aggregate and compare aerial survey and SAR image data, image segments representing zones of homogeneous sea ice, called objects, were created along the survey track following Nasonova *et al*. 2017. Specifically, two sequential Sentinel-1 C-band SAR scenes covering the entire study area were used to create objects. The Sentinel-1 images are freely available from the Copernicus Open Access Hub. From these scenes, the sigma-nought calibrated and Lee speckle filtered (7 x 7 window) HH-polarization bands were processed in the object-based image analysis (OBIA)-driven software eCognition (Trimble) [Table 3.1; Figure 3.1]. Objects were created based on user defined criteria, including a scale criterion, which controls the object size, spatial heterogeneity, which is related to the shape of the object, and spectral heterogeneity, which describes the variance of data within the objects (Benz *et al.* 2004). OBIA is advantageous for analysis of homogeneous portions of sea ice and integration of multisensor data for inter-comparisons when compared to gridded approaches commonly used in the analysis of remote sensing imagery (Nasonova *et al.* 2017).

Within the region of study, 169 objects were generated with an average area of 1100 $m^2$. The segmented objects were manually labelled according to their dominant ice class present within the object, as appearing in the base Sentinel-1 image used to create the objects, i.e. LFYI ($n$ = 67) or DFYI ($n$ = 102). The segmented objects were overlaid on the aerial survey track, and coincident RADARSAT-2 and PALSAR-2 images. As PS1 was acquired northeast of the other images, the objects used to sample image and airborne survey data differ from the objects associated with the other images. The ice

objects overlaid on PS1 were more heavily deformed and there was significantly less LFYI objects than DFYI.

For each object, laser scanner measured $s_{rms}$, ice thickness ($H_{ice}$), and melt pond fraction ($f_p$) were extracted. Backscatter statistics (minimum, maximum, mean, range, standard deviation) were calculated from intensity values, then converted into decibels (dB) for analysis and presentation. There was an average of 290 pixels sampled per image object, ranging from 32 to 1031 pixels, to create backscatter statistics. For correlation and regression analysis, the $s_{rms}$ measurements were transformed to logarithmic values since the un-transformed data follow a lognormal distribution.

Pearson's correlation coefficients (r) were calculated between the profiles of surface parameters (i.e. ice thickness, surface roughness, and melt pond fraction) to examine inter-relationships. Correlation testing was also used to evaluate relationships between the object-wise mean backscatter parameters, and laser scanner measured surface roughness. An ordinary least squares (OLS) regression analysis was performed with SAR backscatter as the independent variable and surface roughness as the dependent variable. For the OLS, a linear function was fitted to the roughness and backscatter, however, since the $s_{rms}$ measurements were transformed to logarithmic values, the modelled regression presented are equivalent to a logarithmic regression model performed on the original $s_{rms}$ data. Based on the regression analysis, surface roughness retrievals models were developed and applied to the SAR imagery to generate modelled surface roughness maps of the region.

This study and prospective relationships touch upon issues of spatial resolution, radar incidence angle, frequency, polarization. The incidence angle effect at L-band

frequency could not be assessed due to the limited range of angles made available by the acquired scenes. However, variations of less than 10° are expected to have minimal influence on the backscatter signal from sea ice (Onstott 1992; Moen *et al.* 2015; Fors *et al.* 2016; Mahmud *et al.* 2018).

## 3.3. Results

### 3.3.1. Ice Conditions

Object-wise mean values of along-track surface parameters $H_{ice}$, $s_{rms}$, and $f_p$ are shown in Figure 3.4, and their distributions are shown in Figure 3.5. The average $s_{rms}$ aggregated within objects ranges from 0.044 m to 0.63 m, however, the non-aggregated $s_{rms}$ varies between 0.028 m to 2.61 m. As anticipated, DFYI has the highest $s_{rms}$ (0.28 m), the highest mean thickness ($H_{ice}$=3.05 m), and the lowest mean melt pond fraction ($f_p$=0.08). LFYI has a lower degree of surface roughness ($s_{rms}$=0.14 m), a smaller average thickness ($H_{ice}$=2.3 m), and higher average pond fraction ($f_p$=0.34).

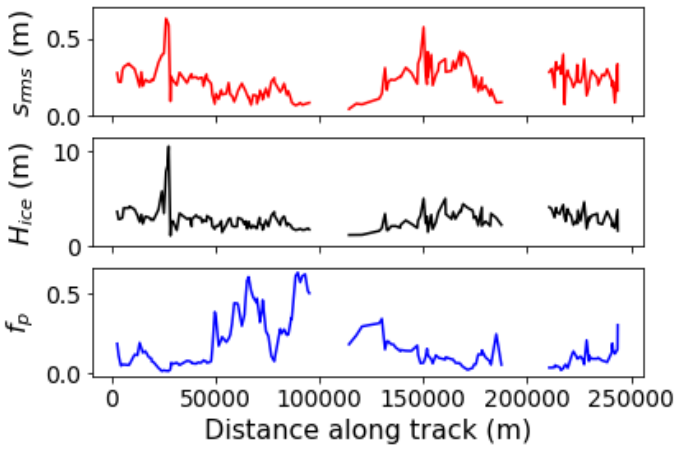


Figure 3.4. Along-track profiles of object-wise mean values of surface parameters: the surface roughness ($s_{rms}$) (top), thickness ($H_{ice}$) (middle), and melt pond fraction ($f_p$) (bottom).

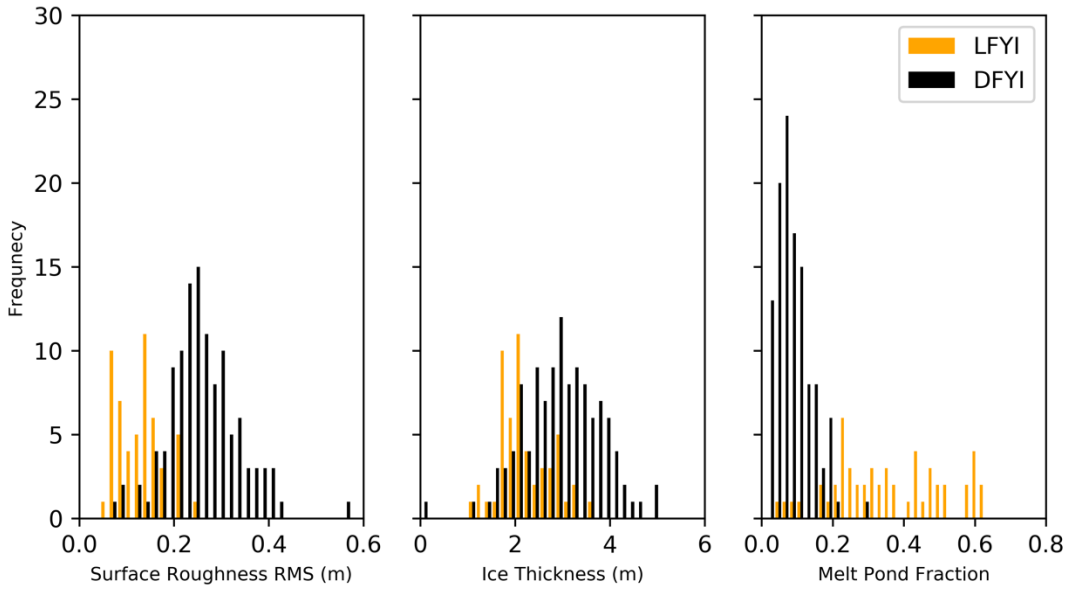


Figure 3.5. Distributions of winter sea ice surface roughness [left] and winter sea ice thickness [middle], and melt pond fraction [right]. LFYI is shown in orange and DFYI in black.

Relationships between sea ice geophysical parameters can be seen in Figure 3.6. The correlation between $f_p$ and $s_{rms}$ is significantly negative, with increasing winter $s_{rms}$ correlating with decreasing advanced melt $f_p$ ($r = -0.65$). This is consistent with previous work that established a strong relation between pre-melt $s_{rms}$ and $f_p$, suggesting that thin and smooth ice is favourable for a high $f_p$, whereas rougher and thicker ice would limit melt pond expansion, resulting in a lower $f_p$ (Landy *et al.* 2015). Ice thickness and $f_p$ have a significant negative relationship, where increased thickness correlated with a decreasimg $f_p$ ($r = -0.45$). Finally, $s_{rms}$ and ice thickness are strongly positively correlated, whereby thicker ice is also rougher ($r = 0.78$). This supports the hypothesis that the development of mean late-winter thickness, especially in FYI, is controlled by dynamic deformation processes, such as ridging, as all level ice is subject to the same growth

conditions during winter and therefore has near-constant thickness (Peterson *et al.* 2008; Toyota *et al.* 2010).

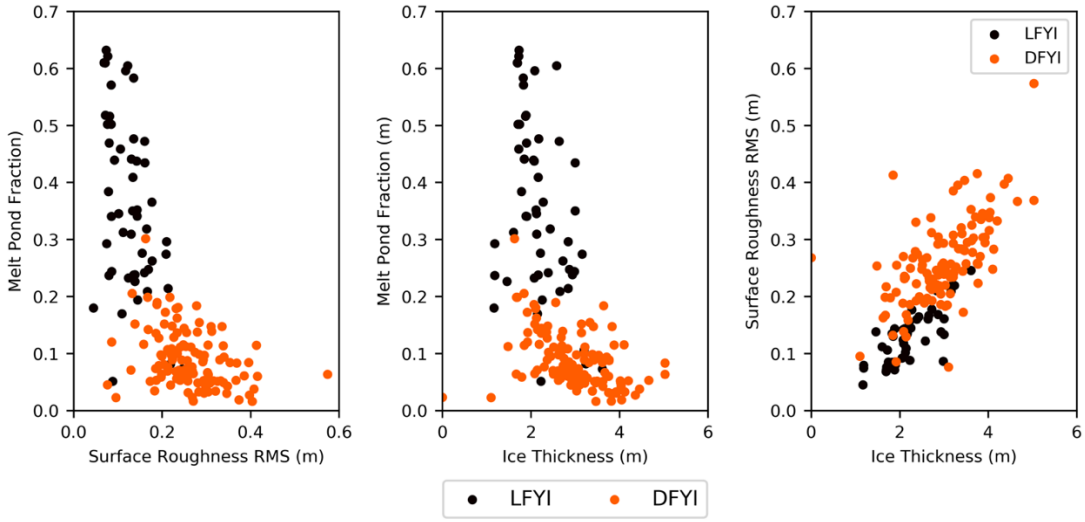


Figure 3.6. Relationships between winter sea ice surface roughness and melt pond fraction [left] and winter sea ice thickness and melt pond fraction [middle], and ice thickness and surface roughness [right]. LFYI is shown in orange and DFYI in black.

### 3.3.2. Correlation and Regression Model: Winter

Correlations between $s_{rms}$ and backscatter coefficients (HH, HV, VH, VV), and $s_{rms}$ and polarimetric ratios ($R_{HV/HH}$ and $R_{VV/HH}$) for winter scenes are given in Table 3.2. Correlations in Tables 3.2 are restricted to data points, i.e. objects, falling within the limits of each scene, and delimited by LFYI and DFYI separately. The highest correlations between $s_{rms}$ and backscatter are found for RS1 ($r$=0.86) and PS1 ($r$=0.82) in winter.

In winter, it was observed that similar relationships arise between $s_{rms}$ and backscatter from the C-band scene taken at shallow incidence angle (RS1), and the L-

band scene at a moderate incidence angle (PS1). Backscatter from these images is strongly and positively correlated with $s_{rms}$ at all four polarizations ($r > 0.75$). Correlations between backscatter and $s_{rms}$ are generally stronger for LFYI compared to DFYI. Within both RS1 and PS1 scenes, slightly higher correlations are observed at co-polarization channels compared to cross-polarization channels. Polarimetric ratios from PS1 are both negatively correlated with $s_{rms}$ for all ice samples ($r_{HV/HH} = -0.65$, $r_{VV/HH} = -0.68$), though the correlations by ice sub-type show a stronger correlation with LFYI compared to DFYI. Although low correlations are observed between polarimetric ratios from RS1 and $s_{rms}$, interestingly, a strong relationship between $R_{HV/HH}$ and $s_{rms}$ ($r = 0.78$) exists for the steep incidence angle RS2 scene. This correlation could be attributed to a stronger sensitivity of $R_{HV/HH}$ to the $s_{rms}$ of DFYI. The effect of incidence angle ($\theta$) between backscatter and $s_{rms}$ is evident for the C-band frequency, as the shallow incidence angle provides much better overall agreement with $s_{rms}$.

Table 3.2. Pearson's correlation coefficients (r) between rms surface roughness, and backscatter coefficients and polarimetric ratios during winter. Correlations are presented according to all samples (All) and by deformation state (LFYI and DFYI). Correlations greater than 0.6 are bolded. A 95% confidence interval was used to evaluate the significance. All correlations are significant unless otherwise noted.

| | **RS1** | | | **RS2** | | | **PS1** | | |
|---|---|---|---|---|---|---|---|---|---|
| | **ALL** | **LFYI** | **DFYI** | **ALL** | **LFYI** | **DFYI** | **ALL** | **LFYI** | **DFYI** |
| $\sigma_{HH}$ | **0.86** | **0.74** | **0.69** | 0.30 | 0.54 | -0.0i | **0.82** | **0.74** | **0.63** |
| $\sigma_{HV}$ | **0.80** | **0.69** | 0.54 | **0.63** | **0.67** | 0.26[i] | **0.75** | **0.65** | 0.55 |
| $\sigma_{VH}$ | **0.82** | **0.68** | 0.57 | **0.63** | **0.69** | 0.25[i] | **0.79** | **0.65** | **0.62** |
| $\sigma_{VV}$ | **0.85** | **0.73** | **0.67** | 0.34 | **0.60** | -0.06 | **0.82** | **0.71** | **0.63** |
| $R_{HV/HH}$ | 0.41 | -0.09 | 0.24 | **0.78** | 0.55 | **0.70** | **-0.65** | **-0.79** | -0.24[i] |
| $R_{VV/HH}$ | 0.15[i] | -0.17[i] | 0.10[i] | 0.62 | 0.50 | 0.37 | **-0.68** | **-0.82** | -0.37 |

[i] non-significant relationship

Regression plots for selected backscatter parameters from scenes PS1 and RS1 are shown in Figure 3.7. The highest $R^2$ was found for RS1, where HH-backscatter was found to explain 72% of the variability in $s_{rms}$. The HH-backscatter in PS1 could explain 67% of the variability in $s_{rms}$.

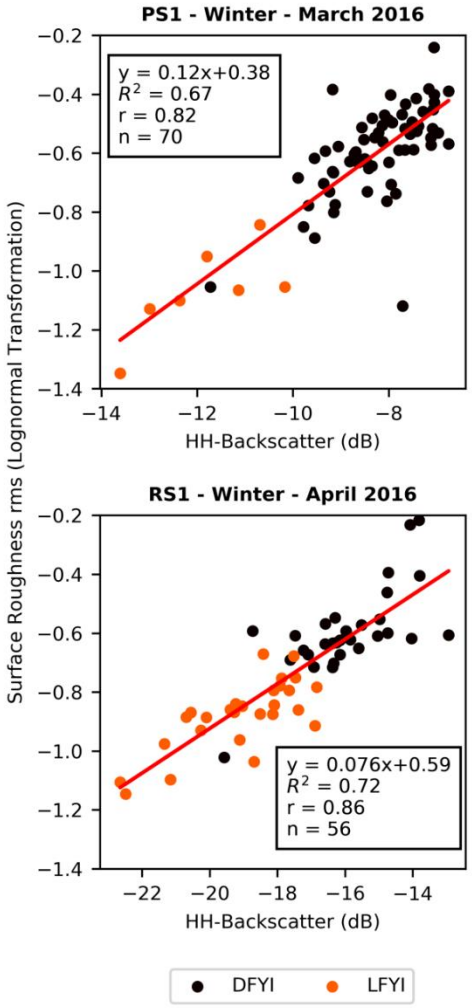


Figure 3.7. Linear OLS model of SAR backscatter as a function of logarithmic surface roughness rms for scenes PS1 and RS1. A linear function has been fitted to the data (solid red line). Corresponding $R^2$, r values, and predictive equations are noted in bottom right corner of each plot. Due to the logarithmic transformation of the $s_{rms}$ data, the modelled outputs ($s_{ln}$) were converted to true surface roughness measurements by means of an exponential function.

Two images and the corresponding maps of estimated surface roughness are shown in Figures 3.8 and 3.9. These are generated using the respective regression equations indicated in Figure 3.7. The largest class (0.6+ m) is restricted based on the input $s_{rms}$ from this study, however, $s_{rms}$ values prior to the object-based aggregation were greater, up to 2.6 m. The majority of the pre-aggregation scan lines fall below 0.6 m, therefore classes presented in surface roughness maps are representative of the input data. Figure 3.8 shows the modelled winter surface roughness derived from HH backscatter from the winter PALSAR-2 image (PS1). Figure 3.9 shows modelled winter surface roughness derived from HH backscatter from the winter RADARSAT-2 scene (RS1).

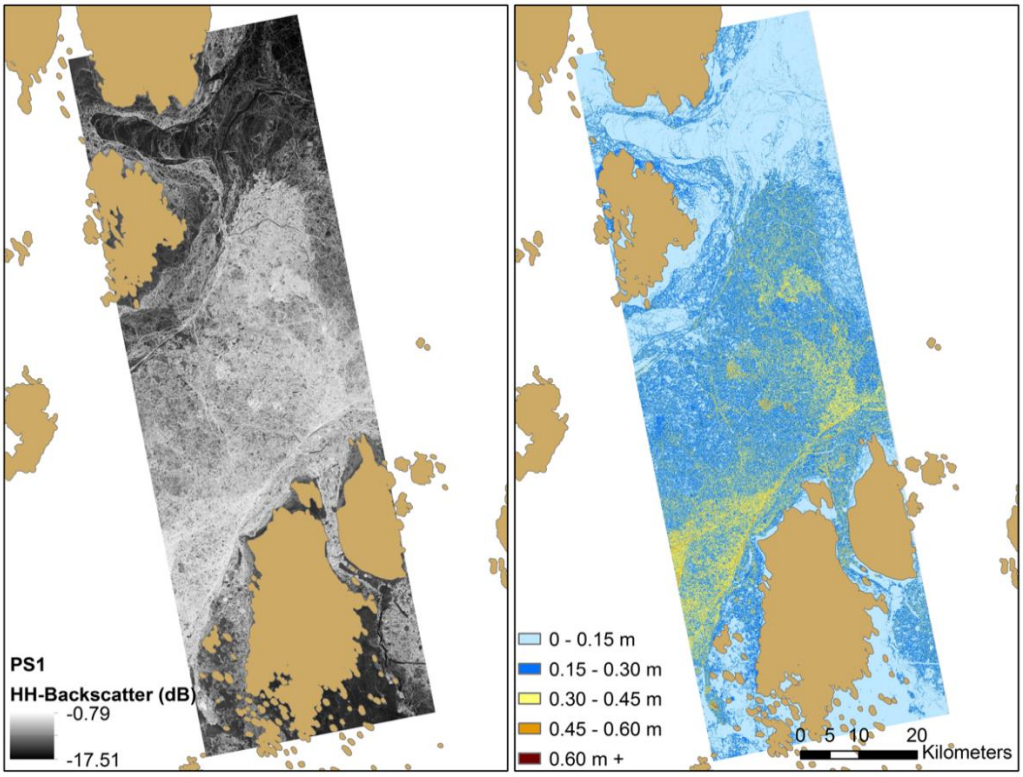


Figure 3.8. Estimated sea ice surface roughness derived from linear regression analysis of HH backscatter from winter PALSAR-2 image (PS1). The original SAR image is presented on the left; and the modelled roughness on the right.

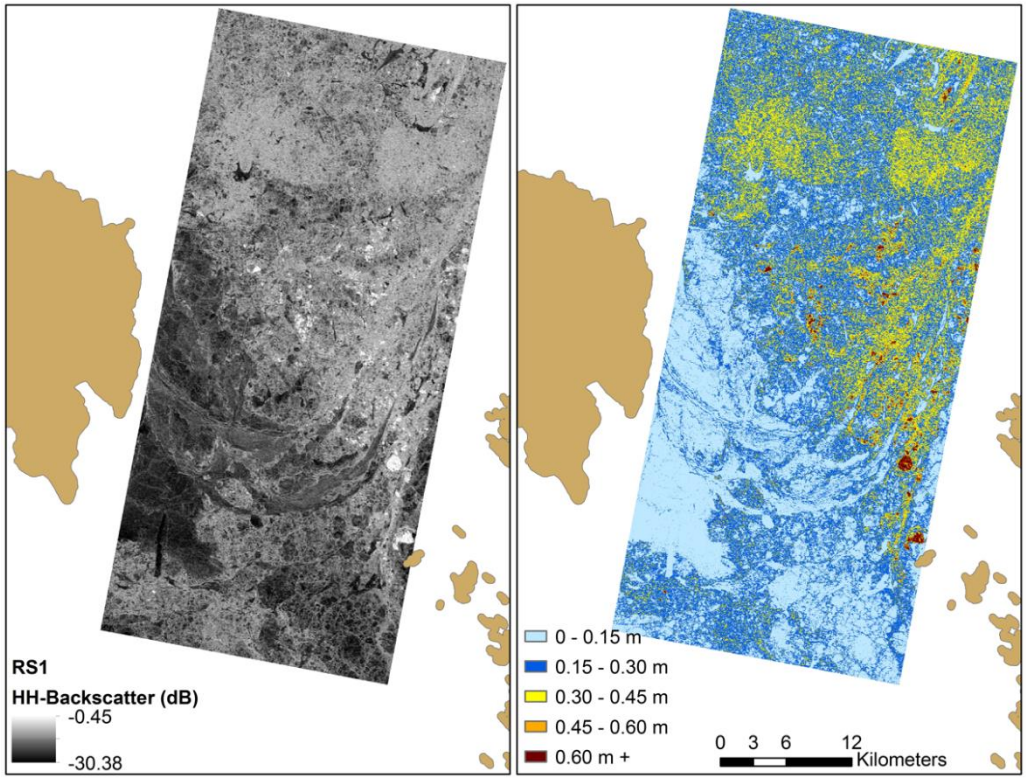


Figure 3.9. Estimated sea ice surface roughness derived from linear regression analysis of HH backscatter from winter RADARSAT-2 scene (RS1). The rough dark red areas are likely MYI floes. This region is primarily older ice and thick FYI. The original SAR image is presented on the left; and the modelled roughness on the right.

Regression residuals are shown in Figure 3.10. Modelled FYI surface roughness shows good agreement with the original laser-scanner derived $s_{rms}$ values; however, both scenes demonstrate significant deviations in DFYI estimates, predominantly when $s_{rms}$ exceeds 0.3 m. Previous studies have identified 0.3 m as a threshold between "smooth" and "rough" ice (e.g. Fors *et al.* 2016). From this analysis, 0.2 m is proposed as an appropriate threshold between LFYI and DFYI [see Figure 3.4]. This is similar to the elevation thresholds used in Castellani *et al.* (2014) and Petty *et al.* (2016) to differentiate between surface features of the ice cover. Both of those studies implemented 0.2 m and 0.8 m thresholds to differentiate between larger sails from smaller sails/snow features.

Lastly, it is important to note that the modelled surface roughness derived from C-band winter imagery is likely skewed due to high volumetric backscatter returns from MYI [see red ice floe in the bottom right corner of Figure 3.8].

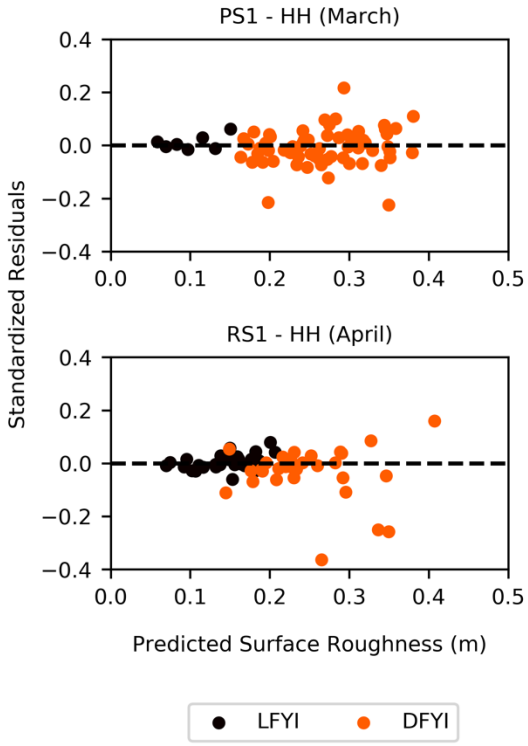


Figure 3.10. Residual plots of predicted surface roughness measurements. Plots are titled by scene.

To validate the derived models, the dataset was divided into approximately equal-sized training and validation subsets. A total of 37 training and 32 validation objects were derived from PS1, and 31 training and 25 validation objects were derived from RS1. An RMSE of 0.07 m was calculated for the RADARSAT-2 HH model and an RMSE of 0.05 m for the PALSAR-2 HH model. Overall, the regression analysis demonstrates that winter backscatter at C- and L-band frequency is useful for predicting the surface

roughness of FYI and hence the deformation state of sea ice in the Canadian Arctic Archipelago. Although backscatter values cannot be associated with direct height measurements, backscatter is largely dependent on variations in height and can be used as an estimate for surface roughness.

### 3.3.3. Correlation and Regression Model: Advanced Melt

Correlations between $s_{rms}$ and backscatter coefficients (HH, HV, VH, VV), and $s_{rms}$ and polarimetric ratios ($R_{HV/HH}$ and $R_{VV/HH}$) for advanced melt scenes are given in Table 3.3. As expected, the relationships established between C-band backscatter at specific polarizations and $s_{rms}$ in winter did not consistently persist into the advanced melt period due to the influence of melting sea ice conditions on SAR measured backscatter. However, it is notable that the HH-band and both polarimetric ratios from the shallow incidence angle RS4 are all strongly correlated with $s_{rms}$. Relationships between $s_{rms}$ and backscatter parameters at L-band did persist; all four polarization channels have an $r > 0.7$, with the highest correlation at HH (0.79). Higher agreement is achieved between $s_{rms}$ and the co-polarization channels in PS2 for LFYI and all ice samples together, though highest correlations for DFYI are found in RS4. In addition, the *co-polarization* ratio from PS2 demonstrates a strong negative relationship with $s_{rms}$ (-0.75).

Table 3.3. Pearson's correlation coefficients (r) between rms surface roughness, and backscatter coefficients and polarimetric ratios during advanced melt. Correlations are presented according to all samples (ALL) and by deformation state (LFYI and DFYI). Correlations greater than 0.6 are bolded. A 95% confidence interval was used to evaluate the significance. All correlations are significant unless otherwise noted.

| | **RS3** | | | **RS4** | | | **PS2** | | |
|---|---|---|---|---|---|---|---|---|---|
| | **ALL** | **LFYI** | **DFYI** | **ALL** | **LFYI** | **DFYI** | **ALL** | **LFYI** | **DFYI** |
| $\sigma_{HH}$ | -0.22[i] | -0.16 | 0.23 | **0.77** | 0.49 | **0.84** | **0.79** | **0.70** | **0.67** |
| $\sigma_{HV}$ | -0.51 | **-0.65** | -0.07 | -0.04[i] | -0.25[i] | 0.55 | **0.73** | 0.55 | 0.58 |
| $\sigma_{VH}$ | -0.50 | **-0.65** | -0.06 | 0.00[i] | -0.28[i] | **0.68** | **0.72** | 0.52 | **0.68** |
| $\sigma_{VV}$ | -0.26[1] | -0.14 | 0.20 | 0.51 | 0.10[i] | **0.79** | **0.76** | **0.70** | **0.65** |
| $R_{HV/HH}$ | -0.53 | **-0.64** | -0.34 | **-0.83** | **-0.63** | **-0.77** | -0.51 | -0.56 | -0.46 |
| $R_{VV/HH}$ | -0.45 | -0.17 | -0.24 | **-0.81** | **-0.59** | **-0.80** | **-0.75** | -0.39 | **-0.65** |

[i] non-significant relationship

The effect of $\theta$ on backscatter and $s_{rms}$ relationships is also apparent when comparing the two C-band images from advanced melt. In terms of backscatter coefficients, the shallow incidence angle (RS4, centre $\theta = 41°$) shows strong correlation between $s_{rms}$ and co-polarization backscatter, with a stronger relationship observed for DFYI compared to LFYI. Whereas, for the steeper incidence angle (RS3, centre $\theta = 23°$), the relationship between cross-polarization channel backscatter and $s_{rms}$ is strongly negative and predominantly influenced by LFYI. RS4 has much higher and consistent correlations for both ratio channels and HH-backscatter across all ice types. The *cross-polarization* and the *co-polarization* ratio channels in RS4 produce the highest correlation between scenes acquired in the advanced melt season ($r_{HV/HH} = -0.83$, $r_{VV/HH} = -0.81$). Regression plots for selected backscatter parameters (PS2 – HH and RS4 HV/HH) are shown in Figure 3.11. The highest $R^2$ was found for PS2, where HH-backscatter was found to explain 62% of the variability in $s_{rms}$. The HV/HH ratio in RS4 could explain 61% of the variability in $s_{rms}$.

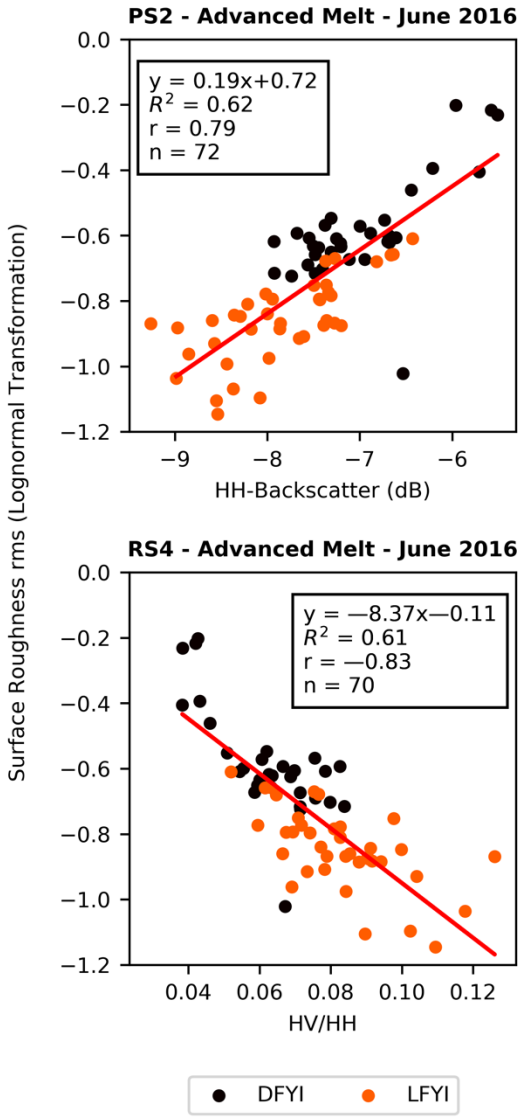


Figure 3.11. Linear OLS model of SAR backscatter as a function of logarithmic surface roughness rms for scenes PS2 and RS4. A linear function has been fitted to the data (solid red line). Corresponding $R^2$, r values, and predictive equations are noted in bottom right corner of each plot. Due to the logarithmic transformation of the $s_{rms}$ data, the modelled outputs ($s_{ln}$) were converted to true surface roughness measurements by means of an exponential function.

Two images and the corresponding maps of estimated surface roughness are shown in Figure 3.12. These are generated using the respective images and regression

equations in Figure 3.11. The classes were created based on the same criteria as the winter regression models in Figure 3.8 and 3.9.

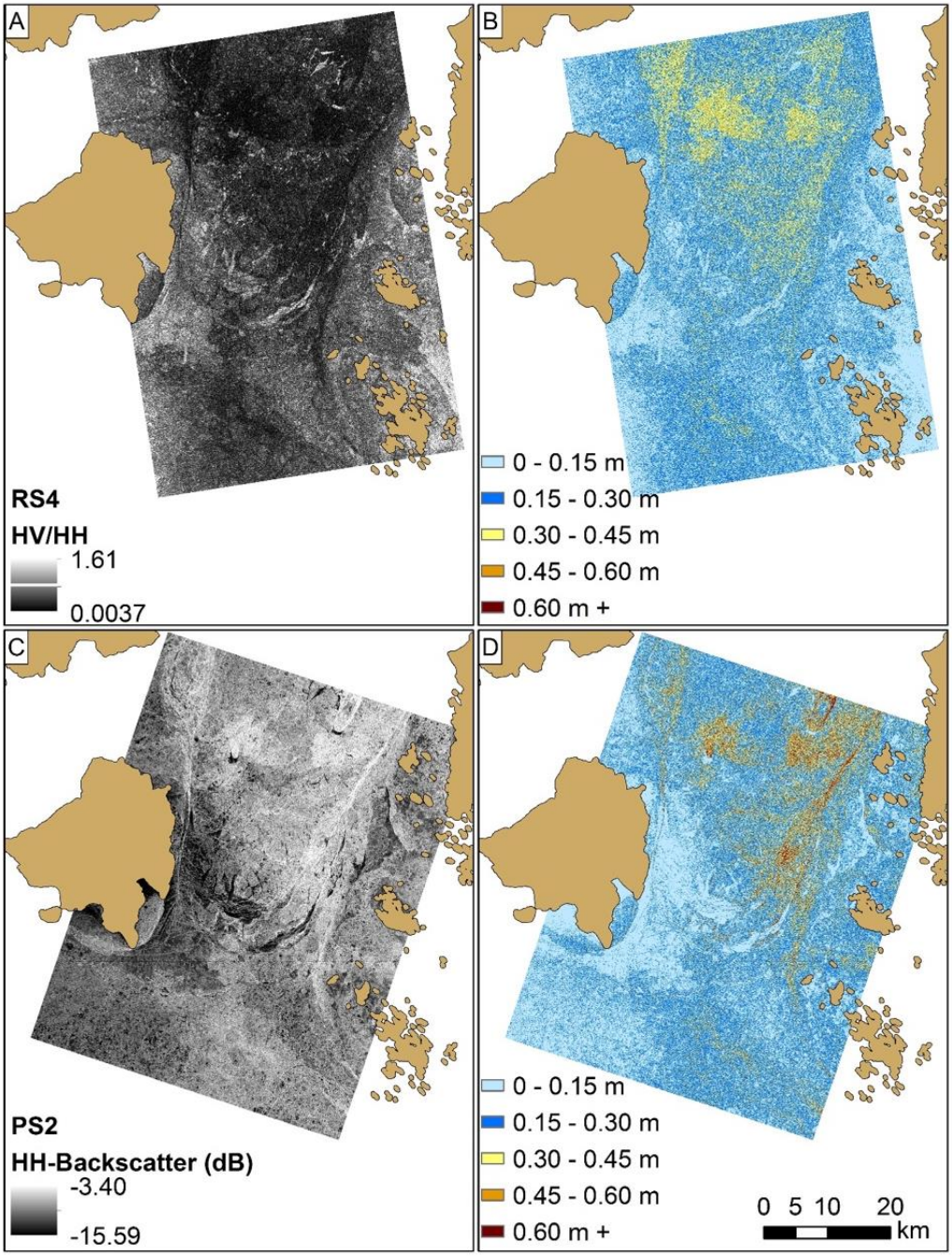


Figure 3.12. Estimated sea ice surface roughness derived from linear regression analysis of HV/HH ratio from advanced melt RS4 (top) and from advanced melt PS2 (bottom). The original SAR images are presented on the left; and the modelled roughness on the right.

Regression residuals are shown in Figure 3.13. In parallel to the winter roughness models, the advanced melt modelled FYI surface roughness shows good agreement with the original laser-scanner derived $s_{rms}$ values and both scenes demonstrate significant deviations in DFYI estimates, predominantly when $s_{rms}$ exceeds 0.3 m.

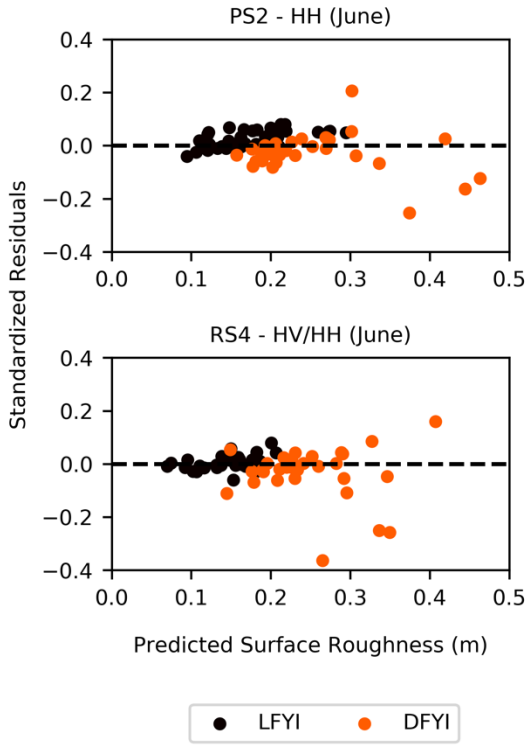


Figure 3.13. Residual plots of predicted surface roughness measurements. Plots are titled by scene.

To validate the derived models, the dataset was divided into approximately equal-sized training and validation subsets. A total of 34 training and 33 validation objects were derived from RS4, and 36 training and 36 validation objects were derived from PS2. An

RMSE of 0.08 m was calculated for the RADARSAT-2 HV/HH model and an RMSE of 0.09 m for the PALSAR-2 HH model.

## 3.4. Discussion

### 3.4.1. Backscatter Coefficients and Polarimetric Ratios

Generally, backscatter is correlated with $s_{rms}$ at both C- and L-band frequencies, with the exception of the C-band scene taken at a steep incidence angle [Table 3.2]. In general, HH-polarization backscatter is the most promising for sea ice surface roughness estimation from both C- and L-band SAR scenes collected during the winter period, provided steep incidence angle C-band scenes are avoided. In usable cases, HH increases in magnitude with increased surface roughness [Figure 3.7; Figure 3.8].

Looking at the polarimetric ratios, it is apparent that $R_{HV/HH}$ is a useful predictor of roughness in C-band imagery acquired at shallow incidence angles. $R_{HV/HH}$ provides an estimate of depolarization so that, in theory, the *cross-polarization* ratio is related to surface roughness, as surface roughness is presumed to be an important contributor to the depolarization of the SAR signal (Drinkwater *et al.* 1992; Fors *et al.* 2016). Therefore, $R_{HV/HH}$ is generally expected to increase with increasing surface roughness. However, our findings only show a positive relationship with roughness in the two winter C-band scenes.

The *co-polarization* ratio is negatively correlated with $s_{rms}$ in all scenes apart from the C-band winter scenes. This polarization ratio has not yet been well established as an indicator of surface roughness at the scale of investigation. Hossain *et al.* (2014) found that the *co-polarization* channel was not able to distinguish between level and deformed

ice. However, their roughness classes were derived from a three-component scattering model. The ratio at C-band has otherwise been readily related to thin ice thickness and melt pond fraction (Scharien *et al.* 2010; Scharien *et al.* 2014). Scharien *et al.* (2014) concluded that $R_{VV/HH}$ could allow quantitative melt pond fraction retrievals over smooth FYI, where deformation is not present. In this case, the ratio is independent of roughness and dependent on the permittivity of the medium, thus the dielectric constants of water and ice. A number of studies have observed a decrease in the *co-polarization* ratio with increased thin ice thickness (Drinkwater *et al.* 1991; Onstott 1992; Nghiem and Bertoia, 2001; Geldsetzer and Yackel 2009; Zhang *et al.* 2016). Correlations between ice thickness and the *co-polarization* ratio are attributed to the changing dielectric constants of the ice surface due to desalination during growth (Zhang *et al.* 2016).

### 3.4.2. Incidence Angle

Backscatter intensity from a sea ice surface is largely dependent on the incidence angle of the scene, though the dependency varies according to ice type and environmental conditions (Mäkynen *et al.* 2002; Fors *et al.* 2016). Our study found that a shallow incidence angle has a stronger sensitivity to surface roughness at C-band frequency [Table 3.2; Table 3.3]. The disparities between winter scenes, RS1 and RS2, demonstrate the effects of incidence angle on backscatter from level and rough surfaces. Backscatter from a surface is expected to decrease with increased incidence angle, where the slope of the decrease varies between sea ice types (Onstott 1992). However, some deformation features, like ridges, counter this statement as they are expected to have brighter returns at shallow incidence angles due a higher contrast between the ridge and surrounding level

ice (Melling 1998). Although the backscatter from rougher DFYI objects remains slightly higher at the steep incidence angle, it is indisguisable from LFYI objects. Whereas, the backscatter of DFYI is higher and much more distinguishable from LFYI at a shallower incidence angle.

Mäkynen *et al.* (2002) investigated the incidence angle (19° to 45°) dependence of C-band HH-polarization backscatter using a very large dataset of RADARSAT images. Their study demonstrated that the contrast between level ice and deformed ice increases with increasing incidence angle, in agreement with our findings. Their study also concluded that backscatter signatures from level ice have a much greater dependency on incidence angle; a rougher surface makes backscatter more random, hence the dependency on incidence angle decreases with increasing surface roughness. However, it was found that HH-polarization correlation of DFYI in C-band has a greater dependency on incidence angle than LFYI objects [Table 3.2]. The difference between studies could be related to our smaller range of incidence angles as well as, regional differences. The Canadian Arctic FYI in our study is much more saline than the brackish Baltic sea ice studied by Mäkynen *et al.* (2002). In addition, the study suggested that wet ice conditions produce a greater dependency on incidence angle than dry conditions (Mäkynen *et al.* 2002). The correlations between $s_{rms}$ and HH observed in this study confirm the findings of Mäkynen *et al.* (2002), as well as Hossain *et al.* (2014), that a shallow incidence angle better decimates between smooth FYI, rough FYI, and deformed FYI. Our findings extend beyond the HH-polarization to demonstrate discrepancies between incidence angles at other polarizations and for polarimetric ratios. The only instance in which

backscatter measured at a steeper incidence had a significantly better agreement with $s_{rms}$ was the $R_{HV/HH}$ in the RS2 scene.

### 3.4.3. Feature Detection during Advanced Melt

The aerial survey conducted during advanced melt enabled us to assess ponding conditions, as well as enable and evaluate feature detection between frequencies. L-band is understood to improve the delineation of deformed ice features (such as ridges, floes, melt ponds), relative to C-band. Visually, the delineation of features in L-band frequency imagery is unquestionably superior during advanced melt [see Figures 3.14/15]. Relative to C-band frequency, imagery acquired at L-band frequency provides excellent contrast between DFYI and LFYI, and enhanced definition of floe boundaries, during advanced melt conditions [Figures 3.14/15].

These results are in agreement with previous studies which demonstrated that L-band SAR may penetrate the snow and melt layer and provide a more detailed depiction of the sea ice surface during the melt season compared to C-band SAR (Dierking and Skriver 2004; Dierking and Busche 2006; Casey *et al.* 2016). Arkett *et al.* (2008) noted improved boundary delineation and deformed feature detection in L-band relative to C-band imagery of FYI in the Beaufort Sea during melt onset conditions (when the snow is wet); and Casey *et al.* (2016) noted improved delineation of deformed ice features in the Canadian Arctic during advanced melt conditions (when the melt ponds have developed and the snow is saturated).

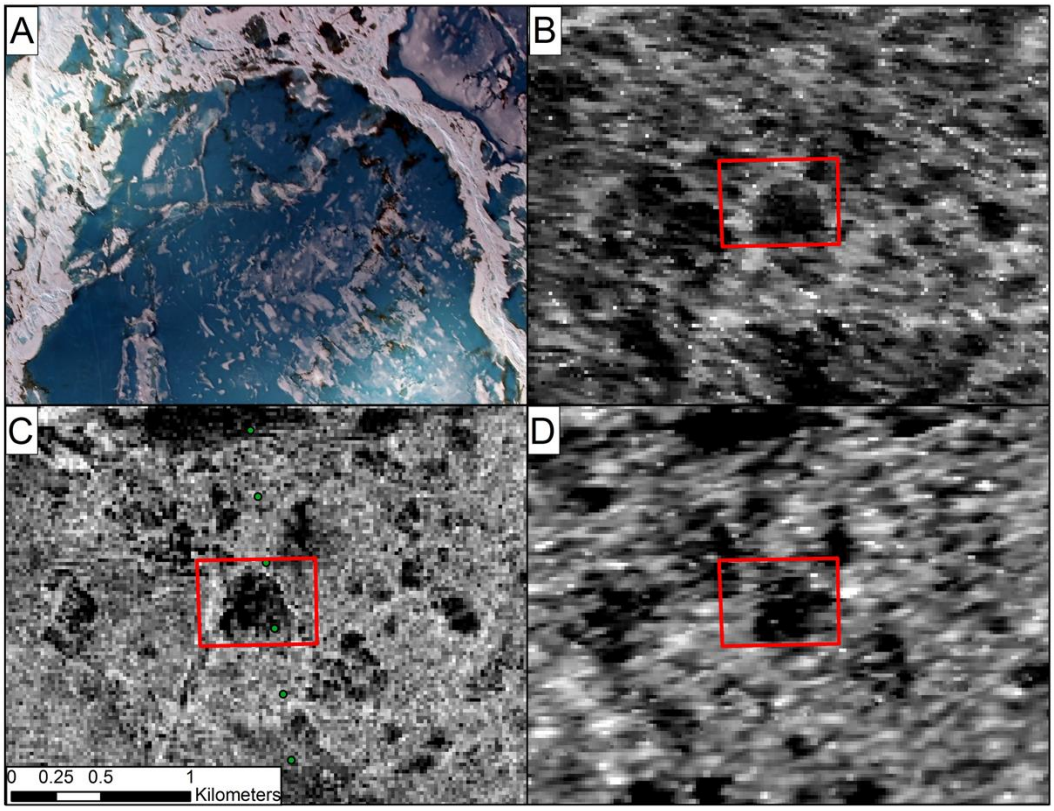


Figure 3.14. Comparisons of ice feature from aerial survey [A] and SAR imagery [B-D]. Scale is only inclusive of SAR imagery. Feature extent is indicated by a red box in SAR imagery. [A] Extensive smooth FYI ponding feature, [B] winter C-band HH-backscatter, [C] advanced melt L-band HH-backscatter, and [D] advanced melt C-band HH-backscatter.

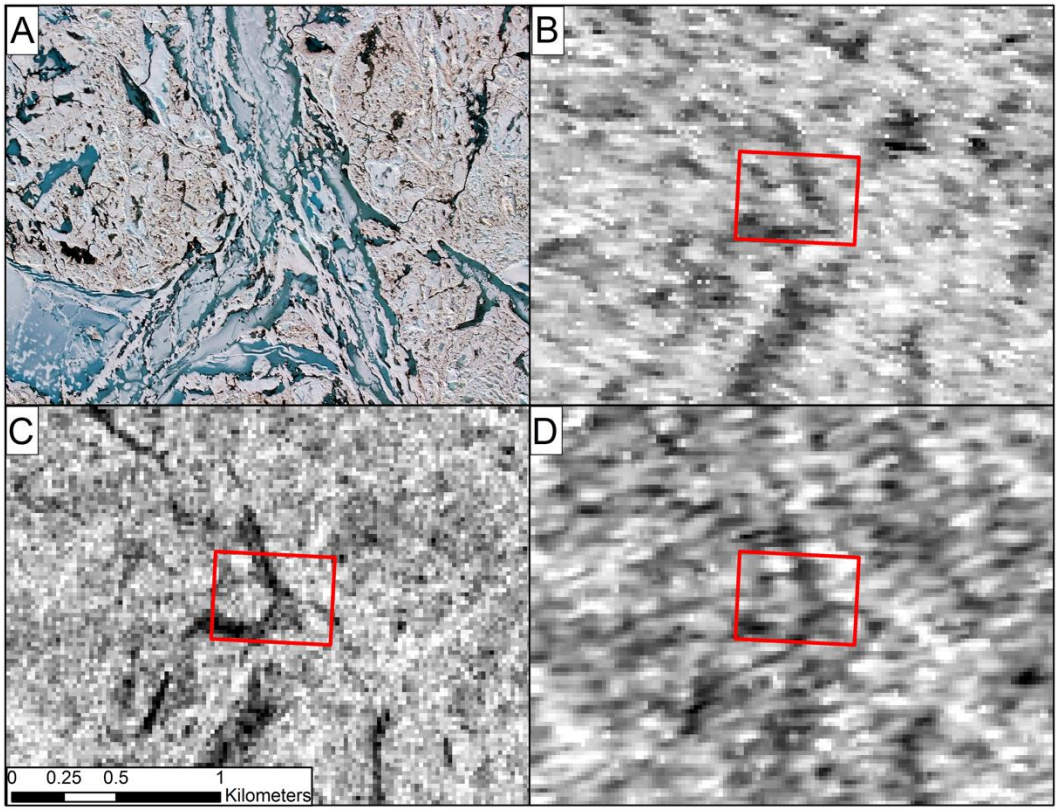


Figure 3.15. Comparisons of ice feature from aerial survey [A] and SAR imagery [B-D]. Scale is only inclusive of SAR imagery. Feature extent is noted by a red box in SAR imagery. [A] flooded smooth FYI feature surrounded by DFYI, [B] winter C-band HH-backscatter, [C] advanced melt L-band HH-backscatter, and [D] advanced melt C-band HH-backscatter.

It is notable that MYI floes are not distinguishable from FYI in C- and L-band imagery acquired during advanced melt conditions [See Figure 3.16], however, are detected in C-band winter imagery due to high volumetric scattering [see Figure 3.9]. This is consistent with other results from Casey *et al.* (2016) where neither C- or L-band provided significant nor reliable separability of these two ice types during advanced melting conditions. The inability to detect MYI during advanced melt is particularly concerning to operational ice services. MYI floes are typically thicker and stronger than FYI floes and can maintain a large portion of their strength during melt conditions (Timco and Johnson, 2004). Lastly our results are similar to Casey *et al.* (2016) who concluded that C-band has a substantially more speckled texture than L-band. The

improved delineation of ice features in L-band could be a result of the reduced speckle. Casey *et al.* (2016) proposed that the reduced speckle in PALSAR-2 data could be attributed to fewer effective scattering centres within each resolution cell at a longer wavelength. The contributions from SAR image properties may also influence the amount of speckle, as the resampled PALSAR-2 image pixels have more independent samples than the resampled RADARSAT-2 image pixels.

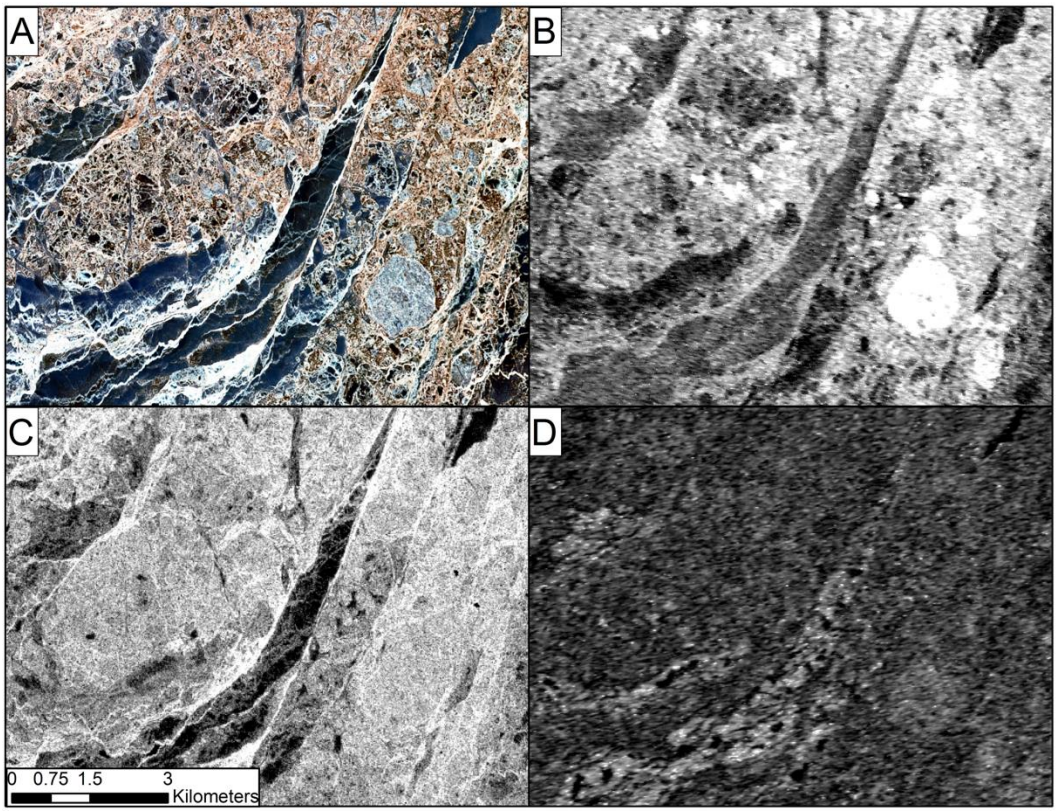


Figure 3.16. Comparison of ice feature detection between C- and L-band. [A] Sentinel-2 (June 14th, 2016) true color image with enhancements to identify MYI floe (light blue) in bottom right corner. Melt ponds are shown by dark blue, [B] winter C-band HH-backscatter, [C] advanced melt L-band HH-backscatter, and [D] advanced melt C-band HH-backscatter.

# Chapter 4 : Thesis Summary and Future Recommendations

This thesis presents quantitative links between sea ice surface roughness and C- and L-band frequency SAR backscatter during winter, as well as advanced melt periods. This was achieved by using a hybrid object-based image analysis to link laser scanner derived surface roughness measurements and spatially coincident SAR backscatter.

The findings presented here demonstrate the utility of both C- and L-band backscatter to retrieve surface roughness estimates in the winter. A winter sea ice surface roughness map derived from SAR imagery provides a more extensive depiction of sea ice surface roughness and topography, which is crucial for estimating atmospheric skin and form drag over Arctic sea ice. Furthermore, the results suggest that L-band can provide a detailed representation of the initial, pre-melt, sea ice surface roughness during advanced melt conditions, as well as demonstrate the potential of C-band imagery (i.e. the *cross-polarization* ratio) to understand the pre-melt first-year ice deformation state even in the presence of melt water. Despite melting conditions, selected backscatter coefficients and ratios are still linked to the winter roughness condition. L-band provides much clearer qualitative observations during the advanced melt as there is less speckle and much more distinct delineation of ice surface features.

Based on the correlation results, recommendations for mapping first-year sea ice surface roughness during winter are: (1) HH-polarization backscatter at C-band frequency ($r=0.86$) and a shallow incidence angle; and (2) HH- or VV-polarization backscatter at L-band frequency ($r=0.82$) and moderate incidence angle. Preferences for understanding the roughness condition of first-year sea ice during advanced melt are: (1) HV/HH polarization ratio at C-band frequency ($r=0.83$) and shallow incidence angle; (2) HH-

polarization backscatter at C-band frequency (r=0.84) and shallow incidence angle (DFYI only); and (3) HH-polarization backscatter at L-band frequency (r=0.79) and a moderate incidence angle.

Quantifying the surface roughness of a natural surface remains challenging due to compromises between point density and extent. The multiscale nature of surface roughness becomes increasingly important and influential when deriving surface roughness parameters from *in situ* and remotely sensed data. There is potential in this, and other studies, that the instrument and sensor limitations impact the results. This study was only concerned with measures of vertical displacement of the surface and excluded the horizontal aspect of surface roughness (Manninen 1997). In addition, averaging the surface roughness among objects results in a loss of surface roughness information. It is however critical to use the object-based aggregation approach for establishing relationships with backscatter that are determined more-so by individual and homogeneous portions of sea ice and less affected by boundaries. Otherwise, the relationships may be noisy or masked due to the different scales of the input data.

It is recommended to design a more in-depth study on the relationship between surface roughness and SAR backscatter during advanced melt. It is necessary to acquire surface roughness measurements during the advanced melt period in order to account for changes in roughness associated with snow erosion and deposition, and snow and ice melt. It is also important to incorporate areas of MYI during both winter and melt analysis. As seen in Chapter 3, the high volumetric backscatter from MYI could influence the model [refer to Figure 3.8 and Figure 3.16]. This study did not have winter L-band imagery covering this MYI ice floe, however, it would be interesting to discern the

relationships between surface roughness of MYI and L-band SAR backscatter.

The strong relationships observed at C-band can be used to derive and explore historical trends due to the continuous dataset at C-band since the establishment of SAR satellites. These relationships, specifically the HV/HH ratio during the melt season, also validate the utility of dual-polarimetric SAR. This is important as many ScanSAR modes covering larger areas provide data solely in the dual-pol acquisition mode, i.e. RADARSAT-2 images used by the Canadian Ice Service and the freely available Sentinel-1 data from ESA. The next logical step is to apply the relationships highlighted in this thesis to Sentinel-1 data. The Sentinel-1 platform has a fairly high temporal resolution and wide coverage, which could enable monitoring of seasonal changes of the ice surface and allow for basin-scale mapping. Lastly, the new RCM set launch this year will provide more polarimetric features, which could possibly improve classification and general observations of sea ice. Future studies should explore the new compact polarimetric data and compare their utility with the traditional dual/quad-polarimetric data.

Sea ice surface roughness models could be used to aid in a suite of tools used for ship navigation, as well as community mapping to identify hazardous and rough areas. It also acts as a key indicator variable in climate models to understand drag coefficients and predict the fate of ice in the summer. SAR imagery is a valuable source of information and provides the most efficient manner to gather regional to basin-scale measurements in the Arctic.

# References

Arkett, M., Flett, D., De Abreu, R., Clemente-Colon, P., Woods, J., and Melchior, B. 2008. "Evaluating ALOS-PALSAR for Ice Monitoring - What Can L-band do for the North American Ice Service?" *IGARSS 2008 – 2008 IEEE International Geoscience and Remote Sensing*, pp. 188-191.

Arya, S. P. S. 1973. "Contribution of form drag on pressure ridges to the air stress on Arctic ice." *Journal of Geophysical Research*, 78(30), pp. 7092–7099.

Arya, S. P. S. (1975). "A drag partition theory for determining the large-scale roughness parameter and wind stress on the Arctic pack ice." *Journal of Geophysical Research*, 80(24), pp. 3447–3454.

Barber, D.G., LeDrew, E.F., Shokr, M., and Falkingham, J. 1992. "Seasonal and diurnal variations in SAR signatures of landfast sea ice." *IEEE Transactions on Geoscience and Remote Sensing*, 30(3), pp. 638-642.

Barber, D.A. and Yackel, J.J. 1999. "The physical, radiative and microwave scattering characteristics of melt ponds on Arctic landfast sea ice." International *Journal of Remote Sensing*, 20(10), pp. 2069-2090.

Barber, D. G., and Nghiem, S. V. 1999. "The role of snow on the thermal dependence of microwave backscatter over sea ice." *Journal of Geophysical Research*, 104(C11), 25, pp. 789–25,803.

Beckers, J.F., Renner, A.H.H., Spreen, G., Gerland, S., and Haas, C. 2015. "Sea-ice surface roughness estimates from airborne laser scanner and laser altimeter observations in Fram Strait and north of Svalbard." *Annals of Glaciology*, 56(69), pp. 235-244.

Benz, U.C., Hofmann, P., Willhauck, G., Lingenfelder, I., and Heynen, M. 2004. "Multi-resolution, object-oriented fuzzy analysis of remote sensing data for GIS-ready information." *ISPRS J. Photogramm. Remote Sensing*, 58, pp. 239–258.

Brown, R.D., and Cote, P. 1992. "Interannual variability of land-fast ice thickness in the Canadian High Arctic, 1950-89, *Arctic*, 45, pp. 273-284.

Carlstrom, A. and Ulander, L.M. 1995. "Validation of backscatter models for level and deformed sea-ice in ERS-1 SAR images." *International Journal of Remote Sensing*, 16(17), pp. 3245-3266.

Carsey, F. D. (Ed). 1992. Microwave Remote Sensing of Sea Ice. American Geophysical Union, Washington, DC, USA. [pdf]

Casey, J.A., Howell, S.E.L., Tivy, A., and Haas, C. 2016. "Separability of sea ice types from wide swath C- and L-band synthetic aperture radar imagery acquired during the melt season." *Remote Sensing of Environment*, 174(1), pp. 314-328.

Castellani, G., Lupkes, C., Hendricks, S., and Gerdes, R. 2014. "Variability of Arctic sea-ice topography and its impact on the atmospheric surface drag." *Journal of Geophysical Research: Oceans,* 119(10). pp. 6743-6762.

Comiso, J.C. 2011. "Large decadal decline of the Arctic multiyear ice cover." *Journal of Climate,* 25, pp. 1176-1193.

Comiso, J.C., Meier, W.N., and Gersten, R. 2017. "Variability and trends in the Arctic Sea ice cover: Results from different techniques." *Journal of Geophysical Research: Oceans,* 122(8).

CSA. 2011. *Satellite characteristics*. Retrieved from http://www.asc-csa.gc.ca/eng/satellites/radarsat/radarsat-tableau.asp

Curry, J.A., Schramm, J.L., Perovich, D.K., and Pinto, J.O. "Applications of SHEBA/FIRE data to evaluations of snow/snow albedo parameterizations." *Journal of Geophysical Research: Atmosphere,* 106(D14).

Dierking, W. and Carlstrom, A. 1997. "The effect of inhomogeneous roughness on radar backscattering from slightly deformed sea ice." *IEEE Transactions on Geoscience and Remote Sensing,* 35(1), pp.147-159.

Dierking, W. 1999. "Multifrequency scatterometer measurements of Baltic Sea ice during EMAC-95." *International Journal of Remote Sensing,* 20(2), 349-372.

Dierking, W. and Skriver, H. 2004. "What is gained by using an L-band SAR for sea ice monitoring?" *Proceedings of the 2004 Envisat and ERS Symposium, Salzburg, Austrias 6-10 September 2001.* ESA SP-572.

Dierking, W. and Busche, T. 2006. "Sea ice monitoring by L-band SAR: An assessment based on literature and comparisons of JERS-1 and ERS-1 Imagery." *IEEE Transactions on Geoscience and Remote Sensing,* 44(2), pp. 957-970.

Dierking, W. and Dall, J. 2007. "Sea-ice deformation state from synthetic aperture radar imagery-Part 1: Comparison of C- and L-band and difference polarization." *IEEE Transactions on Geoscience and Remote Sensing,* 45(11), pp. 3610-3622.

Dierking, W. 2013. "Sea ice monitoring by Synthetic Aperture Radar." *Oceanography*, 26(2).

Drinkwater, M.R., Kwok R., Winebrenner D.P., and Rignot E. 1991, "Multifrequency polarimetric synthetic aperture radar observations of sea ice." *Journal of Geophysical Research*, 96(C11), pp. 20,679-20,698.

Drinkwater, R. Kwok, E. Rignot, H. Israelsson, R. G. Onstott, and D. P. Winebrenner. 1992. "Potential applications of polarimetry to the classification of sea ice," in *Microwave Remote Sensing of Sea Ice*, F. D. Carsey, Ed. Washington, DC, USA: AGU, 1992, vol. 68, pp. 419–430.

Eicken, H., Grenfell, T.C., Perovich, D.K., Richter-Menge, J.A., and Frey, K. 2004. "Hydraulic controls of summer Arctic pack ice albedo." *Journal of Geophysical Research*, 109(C8), C08007.

Eriksson, L.E.B., Borenas, K., Dierking, W., Berg, A., Santoro, M., Pemberton, P., Lindh, H., and Karlson, B. 2010. "Evaluation of new spaceborne SAR sensors for sea-ice monitoring in the Baltic Sea." *Canadian Journal of Remote Sensing*, 36(1), S56-S73.

ESA. 2016. *Sentinel-1 Product Definition*. Retrieved from https://sentinel.esa.int/documents/247904/1877131/Sentinel-1-Product-Definition

ESA. 2019. *Snow and Ice Overview*. Retrieved from https://earth.esa.int/web/guest/earth-topics/snow-and-ice

Fetterer, F. and Untersteiner, N. 1998. "Observations of melt ponds on Arctic sea ice." *Journal of Geophysical Research*, 103(C11), pp. 24821-24835.

Fors, A.S., Brekke, C., Gerland, S., Dougleris, A.P., and Beckers, J.F. 2016. "Late summer Arctic sea ice surface roughness signatures in C-band SAR data." *IEEE Journal of Selected Topics in Applied Earth Observations and Remote Sensing*, 9(3), pp. 1199-1215.

Gegiuc, A., Similä, M., Karvonen, J., Lensu, M., Makynen, M., and Vainio, J. 2018. "Estimation of degree of sea ice ridging based on dual-polarized C-band SAR data". *Cryosphere*, 12, 343-364.

Geldsetzer, T., and Yackel, J. J. 2009. "Sea ice type and open water discrimination using dual co-polarized C-band SAR." *Canadian Journal of Remote Sensing*, 35, 73–84.

Gill, J.P., Yackel, J.J., and Geldsetzer, T. 2013. "Analysis of consistency in first-year sea ice classification potential of C-band SAR polarimetric parameters." *Canadian Journal of Remote Sensing*, 39(2), pp. 101-107.

Gill, J.P. and Yackel, J.J. 2012. "Evaluation of C-band SAR polarimetric parameters for discrimination of first-year sea ice types." *Canadian Journal of Remote Sensing*, 38(3), pp. 306-323.

Gupta, M., Barber, D.G., Scharien, R.K., and Isleifson, D. 2012. "Detection and classification of surface roughness in an Arctic marginal sea ice zone." *Hydrological Processes,* 28, pp. 599-609.

Gupta, M., Barber, D.G., and Scharien, R.K. 2013. "C-band polarimetric coherences and ratios for discriminating sea ice roughness." *International Journal of Oceanography*, 2013, pp. 1-13.

Haas, C. and Howell, S.E.L. 2015. "Ice thickness in the Northwest Passage." *Geophysical Research Letters,* 42(18), pp. 7673-7680.

Haas, C., Hendricks, S., Eicken, H., and Herber, A. 2010. "Synoptic airborne thickness surveys reveal state of Arctic sea ice cove.", *Geophysical Research Letters*, 37, L09501.

Haas, C., Lobach, J., Hendricks, S., Rabenstein, L., and Pfaffling, A. 2009. Helicopter-borne measurements of sea ice thickness, using a small and lightweight, digital EM system. *Journal of Applied Geophysics*, 67, pp. 234–241.

Herzfeld, U.C., Williams, S., Heinrichs, J., Maslanik, J., and Sucht, S. 2016. "Geostatisical and statistical classification of sea-ice properties and provinces from SAR data." *Remote Sensing,* 8(8), pp.616.

Hilber, W.D. 1979. "A dynamic thermodynamic sea ice model." *Journal of Physical Oceanography,* 9, pp. 815-846.

Hunke, E.C. and Dukowicz, J.K. 1997. "An elastic-viscous-plastic model for sea ice dynamics." *American Meterological Society*.

Hunke, E.C., Lipscomb, W.H., and Turner, A.K. 2010. "Sea-ice models for climate study retrospective and new directions." *Journal of Glaciology,* 56(200), pp. 1162-1172.

Isleifson, D., Galley, R.J., Barber, D.G., Landy, J.C., Komarov, A.S., and Shafai, L. 2013. "A Study on the C-band polarimetric scattering and physical characteristics of frost flowers on experimental sea ice." *IEEE Transactions on Geoscience and Remote Sensing*, 52(3).

JAXA. 2008. *ALOS data users handbook*, revision C, March 2008. Retrieved from http:// www.eorc.jaxa.jp/ALOS/en/doc/fdata/ALOS_HB_RevC_EN.pdf

Johannessen, O.M. Alexandrov, V., Frolov, I.Y., Sandven, S., Pettersson, L.H., Bobylev, L.P., Kloster, K., Smirnov, V.G., Mironov, Y.U., and Babich, N.G. 2007. *Remote Sensing of Sea Ice in the Northern Sea Route.* Berlin, Germany: Springer-Verlag Berlin Heidelberg.

Johansson, A.M, King, J.A., Dougleris, A.P., Gerland, S., Singha, S., Spreen, G., and Busche, T. 2016. "Combined observations of Arctic sea ice with near-coincident collocated C-band, and L-band SAR satellite remote sensing and helicopter-borne measurements." *Journal of Geophysical Research,* 122(1), 669-691.

Kwok, R., and Rothrock, D. A. 2009. "Decline in Arctic sea ice thickness from submarine and ICESat records: 1958–2008." *Geophysical Research Letters*, 36(L15501).

Landy, J.C. , Ehn, J.K., and Barber, D.G. 2015. "Albedo feedback enhanced by smoother Arctic sea ice." *Geophysical Research Letters*, 42, pp. 10714-10720.

Lee, J.S. 1986. "Speckle suppression and analysis for synthetic aperture radar images." *Optical Engineering*, 25(2), pp. 636-643.

Leppäranta, M. 2005. *The Drift of Sea Ice*, Springer, Berlin, 266 p. [pdf]

Lindsay, R.W. and Zhang, J. 2005. "The thinning of Arctic sea ice, 1988-2003: Have we passed a tipping point?" *Journal of Climate,* 83(2), pp. 4879-4894.

Mahmud, M.S., Geldsetzer, T., Howell, S.E.L., Yackel, J.J., Nandan, V., and Scharien, R.K. 2018. "Incidence angle dependence of HH- polarized C- and L-band wintertime backscatter over Arctic sea ice." *IEEE Transactions on Geoscience and Remote Sensing*, 56 (11), 6686-6698.

Mäkynen, M.A., Manninen, A.T., Similä, M.H., Karvonen, J.A., and Hallikainen, M.T. 2002. "Incidence angle dependence of the statistical properties of C-band HH-polarization backscattering signatures of the Baltic Sea ice." *IEEE Transactions of Geoscience and Remote Sensing*, 40(12), pp. 2593–2605.

Manninen, A.T. 1997. "Surface roughness of Baltic sea ice." *Journal of Geophysical Research: Oceans,* 102(C1).

Manes, C., Guala, M., Lowe, H., Bartlett, S., Egli, L., and Lehning, M. 2008. "Statistical properties of fresh snow roughness." *Water Resources Research*, 44, W11407.

Markus, T., Stroeve, J.C., and Miller, J. 2009. "Recent changes in Arctic sea ice melt onset, freezeup, and melt season length." *Journal of Geophysical Research,* 114(C12024).

Martinez-Agirre, A., Álvarez-Mozos, J., Lievens, H., Verhonest, N.E.C., Giménez, R. 2017. "Infleunce of surface roughness sample size for C-band SAR backscatter applications on agricultural soils." *IEEE Transactions on Geoscience and Remote Sensing,* 14(12), pp. 2300-2304.

Maslanik, J., Stroeve, S., Fowler, C., and Emery, W. 2011. "Distribution and trends in Arctic sea ice age through spring 2011." *Geophysical Research Letters,* 38(L13502).

Melling, H. 1998. "Detection of features in first-year ice pack by synthetic aperture radar (SAR)." *International Journal of Remote Sensing*, 19(6), pp. 1223-1249.

Melling, H. 2002. "Sea ice of the northern Canadian Arctic Archipelago." *Journal of Geophysical Research: Ocean,* 107.

Moen, M.A. 2013. "Comparison of feature-based segmentation of full polarimetric SAR satellite sea ice images with manually drawn ice charts." *The Cryosphere,* 7(6), pp. 1693-1705.

Moen, M.A., Anfinsen, S., Dougleris, A., Renner, A., and Gerland, S. 2015. "Assessing polarimetric SAR sea-ice classifications using consecutive day images." *Annals of Glaciology.* 56(69), pp. 285-294.

Morassutti, M.P. and Ledrew, E.F. 1996. "Albedo and depth of melt ponds on sea ice." *International Journal of Climatology,* 16(7), pp. 817-838.

Nasonova, S., Scharien, R.K., Haas, C., and Howell, S.E.L. 2017. "Linking regional winter sea ice thickness and surface roughness to spring melt pond fraction on landfast Arctic sea ice." *Journal of Remote Sensing*, 10(1), 37.

Natural Resource Canada. 2019, April 5. Canada Centre for Remote Sensing. Retrieved from https://www.nrcan.gc.ca/earth-sciences/geomatics/CCRS/21749

NSIDC. 2019. All About Sea Ice. Retrieved from https://nsidc.org/cryosphere/seaice/index.html

NSIDC. 2019. Remote Sensing: Introduction. Retrieved from https://nsidc.org/cryosphere/seaice/study/remote_sensing.html

Nghiem, S. and Bertoia, C. 2001. "Study of Multi-Polarization C-Band Backscatter signatures for Arctic sea ice mapping with future satellite SAR." *Canadian Journal of Remote Sensing,* 5, pp. 387-402.

Onstott, R.G. 1992. "SAR and scatterometer signatures of sea ice, Microwave Remote Sensing of Sea Ice", F. Carsey, Ed. Washington, DC, USA: AGU, vol. 63, pp. 73-104.

Paterson, J.S., Brisco, B., Argus, S., and Jones, G. 1991. "In situ measurements of micro-scale surface roughness of sea ice." *Arctic,* 44, pp. 140-146.

Perovich, D.K., Grenfell, T.C., Light, B., and Hobbs, P.V. 2002. "Seasonal evolution of the albedo of multiyear Arctic sea ice." *Journal of Geophysical Research: Oceans,* 107(C10).

Perovich, D.K. and Polashenski, C. 2012. "Albedo evolution of seasonal Arctic sea ice," *The Cryosphere,* 39(8), L08501.

Peterson, I.K., Prinsenberg, S.J., and Holladay, J.S. 2008. "Observations of sea ice thickness, surface roughness, and ice motion in Amundsen Gulf." *Journal of Geophysical Research,* 113(C6).

Petrich, C. and Eicken, H. 2010. "Growth, structure, and properties of sea ice." Sea Ice, Second Edition. Hoboken, Hoboken, Jew Jersey: Wiley-Blackwell.

Petty, A.A., Tsamados, M.C., Kurtz, N.T., Farrel, S.L., Newman, T., Harbeck, J.P., Feltham, D.L., and Richter-Menge, J.A. 2016. "Characterizing Arctic sea ice topography using high-resolution IceBridge data." *The Cryosphere,* 10, pp. 1161-1179.

Petty, A.A., Tsamados, M., and Kurtz, N.T. 2017. "Atmospheric form drag coefficients over Arctic sea ice using remotely sensed ice topography data, spring 2009-2015." *Journal of Geophysical Research: Earth Surface,* 122(8), pp. 1472-1490.

Richards, J.A. 2009. Remote Sensing with Imaging Radar. Berlin, Germany: Springer.

Rivas, M. B., Maslanik, J. A., Sonntag, J. G., and Axelrad, P. 2006. "Sea ice roughness from airborne LIDAR profiles." *IEEE Transactions on Geoscience and Remote Sensing*, 44 (11), pp.3032–3037.

Rösel, A., Kaleschke, L., and Birnbaum, G. 2012. "Melt ponds on Arctic sea ice determined from MODIS satellite data using artificial neural network." *The Cryosphere,* 6, pp. 431-446.

Rothrock, D.A. and Thornlike, A.S. 2018. "Geometric properties of the underside of sea ice." *Journal of Geophysical Research,* 85, pp, 3955-3963.

Sadeh, Y., Cohn, H., Maman, S., and Blumberg, D.G. 2018. "Evaluation of Manning's n roughness coefficient in arid environments by using SAR backscatter." *Remote Sensing,* 10(10), pp. 1505.

Scharien, R.K., Geldsetzer, T., Barber, D.G., Yackel, J.J., and Langlois, A. 2010. "Physical, dieletric, and C band microwave scattering properties of first-year sea ice during advanced melt," *Journal of Geophysical Research,* 115, C12026.

Scharien, R.K., Hochheim, K., Landy, J., and Barber, D.G. 2014. "First-year sea ice melt pond fraction estimation from dual-polarisation C-band SAR – Part 2: Scaling in situ to Radarsat-2." *The Cryosphere,* 8, pp. 2163-2176.

Schröder, D., Feltham, D.L., Flocco, D., and Tsamados, M. 2014. "September Arctic sea-ice minimum predicted by spring melt-pond fraction." *Nature Climate Change,* 4, pp. 353-357.

Shokr, M. and Sinha, N. 2015. *Sea Ice: Physics and Remote Sensing.* Washington, DC: American Geophysical Union.

Similä, M., Mäkynen, M., and Heiler, I. 2010. "Comparison between C band synthetic aperture radar and 3-D laser scanner statistics for the Baltic Sea ice." *Journal of Geophysical Research,* 115(C10056).

Singha, S., Johansson, M., Hughes, N., Hvidegaard, S.M., and Skourup, H. 2018. "Arctic sea ice characterizations using spaceborne fully polarimetric L-, C-, and X-band SAR with validation by airborne measurements." *IEEE Transactions on Geoscience and Remote Sensing,* 56(7), 3715-3734.

Steiner, N., Harder, M., and Lemke, P. 1999. "Sea-ice roughness and drag coefficients in a dynamic-thermodynamic sea-ice model for the Arctic." *Tellus,* 51A, pp. 964–978.

Stroeve, J.C., Kattsov, V., Barrett, A., Serreze, M., Pavlova, T., Holland, M., and Meier, W.N. 2012. "Trends in Arctic sea ice extent from CMIP5, CMIP3 and observations." *Geophysical Research Letters,* 39(16).

Stroeve, J.C., Markus, T., Boisvert, L., Miller, J., and Barrett, A. 2014. "Changes in Arctic melt season and implications for sea ice loss." *Geophysical Research Letters,* 41(4).

Style, R.W. and Worster, M.G. "Frost flower formation on sea ice and lake ice." *Geophysical Research Letters,* 36(L11501).

Thomas, D.N. 2017. *Sea Ice* (3rd Edition). Hoboken, New Jersey: Wiley-Blackwell.

Timco, G.W. and Johnston, M. 2004. "Ice loads on the caisson structures in the Canadian Beaufort Sea," *Cold regions science and technology,* 38(2-3), pp. 185-209.

Toyota, T., Nakamura, K., Uto, S., Ohshima, K.I., and Ebuchi, N. 2010. "Retrieval of sea ice thickness distribution in the seasonal ice zone from airborne L-band SAR." *International Journal of Remote Sensing,* 30(12), pp. 3171-3189.

Ulaby, F.T., Moore, R.K., and Fung, A.K. 1986. Microwave Remote Sensing: Active and Passive, Vol. 3, From Theory to Applications, Artech House.

Ulaby, F.T., Stiles, W.H., and Abdelrazik, M. 1984. "Snowcover influence on backscatter from terrain." *IEEE Transactions on Geoscience and Remote Sensing*, GE-22(2), pp. 126-132.

von Saldern, C. , Busche, T. , Haas, C. and Dierking, W. 2004. "Analysis of Sea Ice Roughness and Thickness Variation for Improvement of SAR Ice Type Classification," *Proceedings of the 2004 Envisat and ERS Symposium*, 6-10 Sept.2004, Salzburg, Austria. European Space Agency. Compiled by H. Lacoste and L. Ouwehand. SP-572

Wadhams, P. and Davis, N.R. 2000. "Further evidence of ice thinning in the Arctic Ocean." *Geophysical Research Letters*, 27(24).

Weiss, J. and Marsan, D. 2004. "Scale properties of sea ice deformation and fracturing." *Comptes Rendus Physique,* 5(7), pp. 735-751.

WMO. 2010. *Oceans.* Retrieved from https://public.wmo.int/en/search?f[0]=field_cloud_tags%3A280

Williams, F.M., Kirby, C. and Slade, T. 1993. "Strength and Fracture Toughness of First-Year Arctic Sea Ice*"*. Report Tr-1993–12, Institute for Marine Dynamics, NRC Canada.

Zhang, X., Dierking, W., Zhang, J., Meng, J., and Lang, H. 2016. "Retrieval of the thickness of undeformed sea ice from simulated C-band compact polarimetric SAR images." *The Cryosphere,* 10, pp. 1529-1545.

# Appendix

## Copyrighted Material and Author Contribution

Chapter 3 includes content from a paper submitted to the Canadian Journal of Remote Sensing. I processed all data types (i.e. radar imagery, laser scanning data, aerial photography), assisted in designing the study, performed the study and analysis, as well as amalgamated the written document. Randy Scharien led the research design, offered guidance during analysis, and provided thorough editing during the writing process. Torsten Geldsetzer assisted in the research design and edited the final article. Stephen Howell provided RADARSAT-2 images and provided editing during writing process. Christian Haas acquired and provided the laser scanner data and edited the final article. Becky Segal and Sasha Nasonova provided guidance during the data processing and analysis.